Petroleum Science 23 (2026) 3334–3350

Contents lists available at ScienceDirect

Petroleum Science

journal homepage: www.keaipublishing.com/en/journals/petroleum-science

Original Paper

Influence of pore structure on the dynamic response of porous rocks under high strain-rate impact: A mesoscale numerical investigation

Zi-Zhen Wang [a,b,*], Wen-Sheng Zhang [a,b], Yan-Bin Zang [c], Xiao-Ao Liu [d], Wei-Dong Zhou [a,b]

[a] State Key Laboratory of Deep Oil and Gas, China University of Petroleum (East China), Qingdao, 266580, Shandong, China
[b] School of Petroleum Engineering, China University of Petroleum (East China), Qingdao, 266580, Shandong, China
[c] SINOPEC Research Institute of Petroleum Engineering, Beijing, 102200, China
[d] CNPC Engineering Technology R&D Company Limited, Beijing, 102200, China

ARTICLE INFO

Article history:
Received 16 September 2025
Received in revised form
2 March 2026
Accepted 2 March 2026
Available online 5 March 2026

Edited by Jia-Jia Fei

Keywords:
Pore structure
Dynamic mechanics
Split hopkinson pressure bar (SHPB)
Numerical investigation

ABSTRACT

This study establishes a numerical simulation method for modeling the dynamic response of porous rocks under high strain-rate impacts and verifies its robustness, accuracy, and reproducibility. A systematic investigation was conducted to evaluate the effects of four pore structure parameters—porosity, pore size, aspect ratio, and orientation angle—on the dynamic response of rocks. The results indicate that increasing porosity significantly reduces normalized strength (σ_{norm}), dynamic Young's modulus (E_d), and energy dissipation density (U_v), with the degree of weakening influenced by pore geometry. A greater aspect ratio difference leads to higher U_v, suggesting that more flattened pores promote complex fracture development and energy dissipation. Furthermore, the study reveals a coupled mechanism between pore structure and impact loading characteristics: Porosity exerts the most significant control on the rock's impact response under different stress-wave loading conditions, whereas the effects of pore shape and size are comparatively secondary. For strength weakening, non-optimal loading periods (T = 200 or 800 μs) are recommended to avoid the strengthening effect observed at T = 400 μs to improve energy efficiency, the optimal loading period should be selected based on porosity. When porosity is less than 3%, applying an impact stress wave with an amplitude 12 times the rock matrix strength achieves an optimal balance between strength reduction and energy efficiency; when porosity exceeds 5%, an amplitude of 6 times the matrix strength yields superior energy utilization. The findings propose a porosity-driven impact loading design strategy, providing theoretical and quantitative guidance for field-scale engineering applications.

1. Introduction

During long-term geological evolution, rocks are subjected to various processes including sedimentation, metamorphism, weathering, and tectonic stresses, resulting in the development of intricate and multiscale networks of pores and fractures (Kranz, 1983). The spatial distribution, size variability, and morphological characteristics of these pores significantly influence the initiation, propagation, and coalescence of microcracks, thereby controlling macroscopic strength, stiffness, and damage evolution trends. Numerous studies have established a strong negative correlation between porosity and rock strength, which has been widely used to predict compressive strength and Young's modulus (Pan et al., 2023; Li et al., 2024; Xiao et al., 2025). However, it is increasingly evident that porosity and average pore size alone are insufficient to fully characterize the mechanical behavior governed by complex microstructures. Both experimental and numerical findings indicate that rocks with similar porosities but different pore sizes exhibit distinct stiffness and failure modes (Zhao et al., 2024). And the microstructural heterogeneity and fluid saturation exert a synergistic influence on the acoustic–elastic behavior of tight sandstones (Pang et al., 2024). To enhance the

* Corresponding author.
E-mail address: wangzzh@upc.edu.cn (Z.-Z. Wang).
Peer review under the responsibility of China University of Petroleum (Beijing).

https://doi.org/10.1016/j.petsci.2026.03.003
1995-8226/

microstructural description, the pore aspect ratio has been introduced as a key geometric parameter. Queiroz et al. (2025) proposed an effective method for estimating equivalent aspect ratios, significantly improving the accuracy of mechanical property predictions. Studies have demonstrated that increasing pore aspect ratio (i.e., flatter pores) reduces elastic modulus and facilitates crack initiation, especially under dynamic and saturated conditions (Bubeck et al., 2017; Hu et al., 2023). Furthermore, Zhao et al. (2022) utilized fractal dimensions to quantify morphological irregularity and found strong nonlinear effects on shear and tensile strength.

Although extensive efforts have explored the influence of pore structures on static mechanical properties, the understanding of their role under high strain-rate dynamic loading remains limited. Most existing studies have focused on low strain-rate conditions, failing to capture the distinctive mechanisms activated during rapid loading scenarios, such as those encountered in drilling, blasting, hydraulic fracturing, and other impact-prone engineering settings (Wang et al., 2021; Zou et al., 2023; Li et al., 2024). Under dynamic loading, stress wave propagation and superposition lead to different failure patterns and energy dissipation behaviors compared to quasi-static conditions (Wang et al., 2020; Zhou et al., 2020). Therefore, it is critical to elucidate the role of pore geometry in the dynamic mechanical behavior of rocks to enhance engineering safety and optimization. Split Hopkinson pressure bar (SHPB) techniques have been widely employed to investigate this topic, confirming that pore and fracture features play a pivotal role in dynamic response. High-porosity rocks tend to exhibit severe fragmentation and energy dissipation under dynamic loading, leading to reduced strength and unstable stress wave transmission (Hu et al., 2022; Stopka et al., 2024). Variations in crack length and spatial distribution alter crack propagation pathways, resulting in multi-peak stress patterns and diverse failure modes (Kim and Changani, 2016; Song et al., 2022; Du et al., 2023). The interplay between porosity and saturation also significantly affects Young's modulus and peak stress (Chen et al., 2024). However, precise quantification of the effects of specific pore geometries—such as pore size, aspect ratio, and orientation—on dynamic response remains underexplored.

Since the current limitations in quantitatively understanding how pore structure affects the dynamic mechanical response of rocks, the development of novel approaches for simulating and analyzing the mechanical behavior of porous rocks is of critical importance. Due to the inherent heterogeneity of natural pore distributions (Liu and Huang, 2021; Zambrano et al., 2021; Yao et al., 2023; Sulieman et al., 2024; Hu et al., 2025), conventional experimental approaches face significant challenges in establishing clear quantitative relationships between pore geometry and mechanical behavior. On the one hand, natural rocks exhibit multiscale porosity, ranging from micron-sized capillaries to millimeter-scale fractures, with highly irregular spatial distributions, making it difficult to independently control and reproduce geometric parameters during experiments. Although some studies have attempted to investigate local responses using artificial notches or embedded flaws (Li et al., 2017, 2018; Asadi et al., 2023; Pan et al., 2023; Zou et al., 2023), these researches fail to capture the authentic geometry and spatial coupling of natural pore systems, limiting their applicability in multi-parameter sensitivity analyses. On the other hand, under realistic loading conditions, rock failure involves complex dynamic evolution of pores—including closure, expansion, and coalescence—governed by the interplay of stress state, loading rate, and pore connectivity. This complexity is exacerbated under high strain rate loading, where pore structures significantly disturb stress wave propagation and damage accumulation. Yet, existing experimental techniques remain limited in capturing microscale damage initiation and crack evolution paths (Rodríguez and Celestino, 2019; Du et al., 2020; He et al., 2020; Yang et al., 2020). Accordingly, there is a compelling need to employ digital rock physics and numerical modeling approaches that enable the construction of idealized or image-based porous models with controlled boundary and material conditions, while maintaining statistical representativeness and decoupling key geometric parameters.

In numerical modeling and digital rock-based studies, a fundamental prerequisite is the establishment of a well-structured pore parameterization framework that enables the decoupled control of key variables. On the one hand, this requires accurate geometric characterization of pore attributes, such as pore size, aspect ratio, orientation, and spatial distribution (Fredrich, 1999). On the other hand, it is essential to ensure the independent tunability of individual variables to isolate and quantify their respective influences. Currently, common modeling approaches include CT-based reconstruction (Yun et al., 2013; Jiang et al., 2019; Jani et al., 2023; Lang et al., 2024; Pang et al., 2025), voronoi packing models (Gao and Stead, 2014; Liu et al., 2017, 2018; Wang et al., 2021), random field models (Ostoja-Starzewski, 1998; Chen et al., 2019), and image-based pore network modeling (Sadeghnejad and Gostick, 2020). These methods have achieved notable progress in replicating pore-scale heterogeneity, fracture networks, and multiscale pore systems. However, most existing approaches face challenges in simultaneously preserving structural realism and achieving effective decoupling of key pore parameters, thereby limiting their applicability in mechanism exploration and sensitivity analyses.

To overcome the aforementioned limitations, this study introduces a meso-structural reconstruction technique originally developed for concrete modeling into the field of porous rock modeling. A controllable pore generation algorithm was developed, enabling the adjustment of porosity, pore size, aspect ratio, and orientation angle. Based on this algorithm, SHPB-based numerical simulation models were established to investigate rock behavior under high strain-rate loading conditions. A systematic analysis was conducted to explore the influence of pore geometric parameters—including porosity, pore size, aspect ratio, and orientation—on dynamic compressive strength, dynamic Young's modulus, and energy dissipation characteristics. The underlying mechanisms were further elucidated through analyses of crack propagation patterns and failure morphology. In addition, the study examined the effects of stress wave amplitude and loading period on the dynamic response of rocks. This work proposes a novel numerical strategy for investigating the mechanical behavior of porous rocks and provides theoretical insights into rock response mechanisms in petroleum drilling and mining engineering applications.

2. Development of the FEM models of the specimen with parameterized pore structures

Natural rocks contain highly irregular pores. Micro-CT observations show pore shapes spanning from near-spherical to flattened ellipsoids, and both pore-shape anisotropy and orientation exert strong control on strength and failure. Therefore, porosity alone is insufficient; pore geometry must be characterized using aspect ratios and orientation. Following prior analytical and numerical evidence that ellipsoidal aspect ratio and orientation govern stress concentration and effective moduli, each pore is idealized as an ellipsoid defined by semi-axes a, b, c aspect ratios b/a and c/a, and Euler angles (α, β, γ). Pore shape is quantified by $(b/a, c/a)$, covering a continuous spectrum from general ellipsoids ($0.5 \le b/a \le 1.0$, $0.5 \le c/a \le 1.0$) to disk-like pores ($b/a \ge 0.8$, $c/a <$

0.3) and needle-like pores ($b/a = c/a \le 0.3$). This parameterization decouples shape from orientation and provides a compact, physically interpretable control of pore geometry.

For modeling simplicity, we assume: (i) pores are ideal ellipsoids; (ii) pore centers (x_0, y_0, z_0) and orientations are uniformly distributed, whereas the major axis a and aspect ratios b/a and c/a follow normal distributions around prescribed means; and (iii) pores are dry, mutually independent, and non-interconnected. The position of a point P (x_P, y_P, z_P) relative to an ellipsoid is evaluated using the implicit quadratic form f (x_P, y_P, z_P), which can be determined by Eq. (1): $f > 0$ indicates P is outside, $f = 0$ on the surface, and $f < 0$ inside. This point–ellipsoid representation supports interference checking, minimum-distance evaluation, and element assignment during finite-element preprocessing, ensuring robust mesh generation.

$$f(x_P, y_P, z_P) = X\boldsymbol{A}B\boldsymbol{A}^{\mathrm{T}}X^{\mathrm{T}} - 1 \tag{1}$$

where, $X = (x_P - x_0, y_P - y_0, z_P - z_0)$, $B = \mathrm{diag}(1/a^2, 1/b^2, 1/c^2)$,where a, b, c are the long semi-axis, the middle semi-axis and the short semi-axis of the ellipsoid, respectively; $\boldsymbol{A}$ is a 3 × 3 matrix related to the nutation angle α, the precession angle β and the spin angle γ of the ellipsoid. Fig. 1 illustrates how pore shape is controlled via the aspect ratio. Matrix $\boldsymbol{A}$ can be calculated by:

$$\boldsymbol{A} = A_\alpha \times A_\beta \times A_\gamma \tag{2}$$

where, $A_\alpha = \begin{bmatrix} \cos\alpha & \sin\alpha & 0 \\ -\sin\alpha & \cos\alpha & 0 \\ 0 & 0 & 1 \end{bmatrix}$, $A_\beta = \begin{bmatrix} 1 & 0 & 0 \\ 0 & \cos\beta & \sin\beta \\ 0 & -\sin\beta & \cos\beta \end{bmatrix}$, $A_\gamma = \begin{bmatrix} \cos\gamma & \sin\gamma & 0 \\ -\sin\gamma & \cos\gamma & 0 \\ 0 & 0 & 1 \end{bmatrix}$

Based on the above assumptions, a parameterized workflow was developed to construct porous rock specimens (Fig. 2). The procedure includes three steps: (i) randomly generate ellipsoidal pores within a cylindrical domain and record each pore's center coordinates, size parameters, and Euler angles; (ii) implement an element-mapping routine in LS-DYNA to classify each element as matrix or pore according to the stored pore geometry; and (iii) remove elements assigned to the pore space, yielding a porous FEM model with prescribed geometric descriptors.

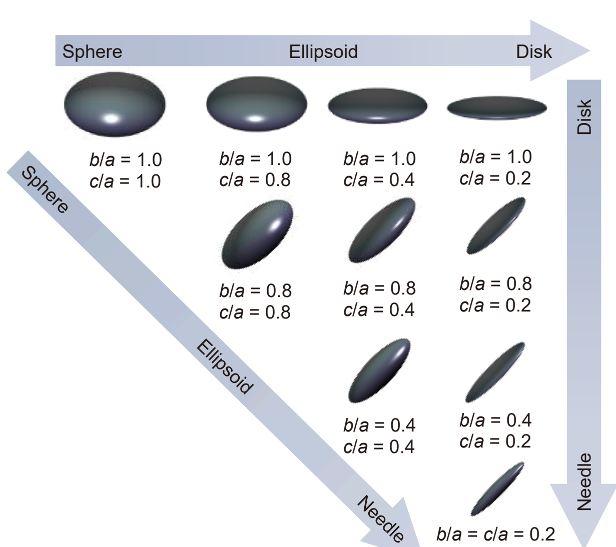

Fig. 1. Shape catalogue of ellipsoidal pores parameterized by aspect ratios b/a and c/a.

The pore-generation algorithm takes the cylinder geometry (R, h), target porosity φ, admissible ranges of (a, b/a, c/a), and the corresponding distribution functions as inputs. Candidate ellipsoids are sampled sequentially from the prescribed distributions and accumulated until the target φ is reached. Each candidate is first subjected to a boundary-avoidance check based on the criteria: $\sqrt{x_0^2 + y_0^2} \le R - a$ and $|z_0| \le h/2 - a$, followed by a pore–pore non-overlap test. Accepted pores are stored as (x_0, y_0, z_0), (α, β, γ), and (a, b, c) for subsequent mesh mapping.

A practical limitation is that the boundary constraint is defined using the maximum semi-axis and therefore does not explicitly account for pore orientation. In a limiting configuration (e.g., the shortest axis aligned radially near the lateral wall), this may produce a thin pore-scarce rim. However, since pore orientations are sampled from uniform distributions, only a small fraction of pores approach such unfavorable boundary alignments, and the resulting porosity reduction in the edge zone is generally much smaller than the theoretical upper bound.

Under random orientation, non-connectivity, and non-overlap constraints, the attainable upper bound of porosity decreases with decreasing aspect ratio. For a fixed a = 0.25 mm, near-spherical ellipsoids (b/a = 0.8, c/a = 0.8) typically allow $\varphi_{\max} \approx$ 30%–40%, disk-like pores (b/a = 0.8, c/a = 0.2) allow $\varphi_{\max} \approx$ 20%–25%, and needle-like pores ($b/a = c/a$ = 0.2) allow $\varphi_{\max} \approx$ 8%–10%. To control the mismatch $\Delta\varphi$ between the prescribed porosity φ_0 and the realized porosity φ_{r} after meshing—particularly for low-aspect-ratio pores where discretization effects are more pronounced—an initial mesh test was performed by prescribing φ_0 = 1%, and measuring φ_{r1}. The prescribed porosity for other target levels was then calibrated using Eq. (3), ensuring that φ_{r} closely matches the design value.

$$\varphi_0 = 1\% \times \frac{\varphi_a}{\varphi_{\mathrm{r1}}} \tag{3}$$

A representative example is shown in Fig. 3. The major semi-axis a and aspect ratios b/a and c/a are independently sampled from truncated normal distributions. The empirical histograms and normal fits (Fig. 3(b)–(d)) agree well with the prescribed distributions, indicating that the generator reliably reproduces the intended first-order statistics under geometric and non-overlap constraints.

Finally, because dense, randomly distributed ellipsoids create complex pore–solid interfaces that hinder body-fitted meshing, a structured hexahedral mesh is generated for the pore-free cylinder first, and pores are introduced by element mapping (Fig. 2(c)). Specifically, the pre-generated node/element lists and the stored pore set—(x_0, y_0, z_0), (α, β, γ), and (a, b, c) are imported, and the inclusion function is evaluated for each element center against all ellipsoids. Elements whose centers fall inside any ellipsoid are classified as pore elements and removed, producing the final porous specimen model.

3. FEM modeling of the SHPB system

3.1. The working principle of the SHPB system

The working principle of the SHPB system is illustrated in Fig. 4. The apparatus consists of a striker bar, an incident bar, and a transmission bar, with the specimen sandwiched between the incident and transmission bars. When the striker impacts the incident bar, a compressive stress pulse is generated and propagates along the bar at the wave velocity. Upon reaching the interface between the incident bar and the specimen, part of the pulse is transmitted through the specimen into the transmission

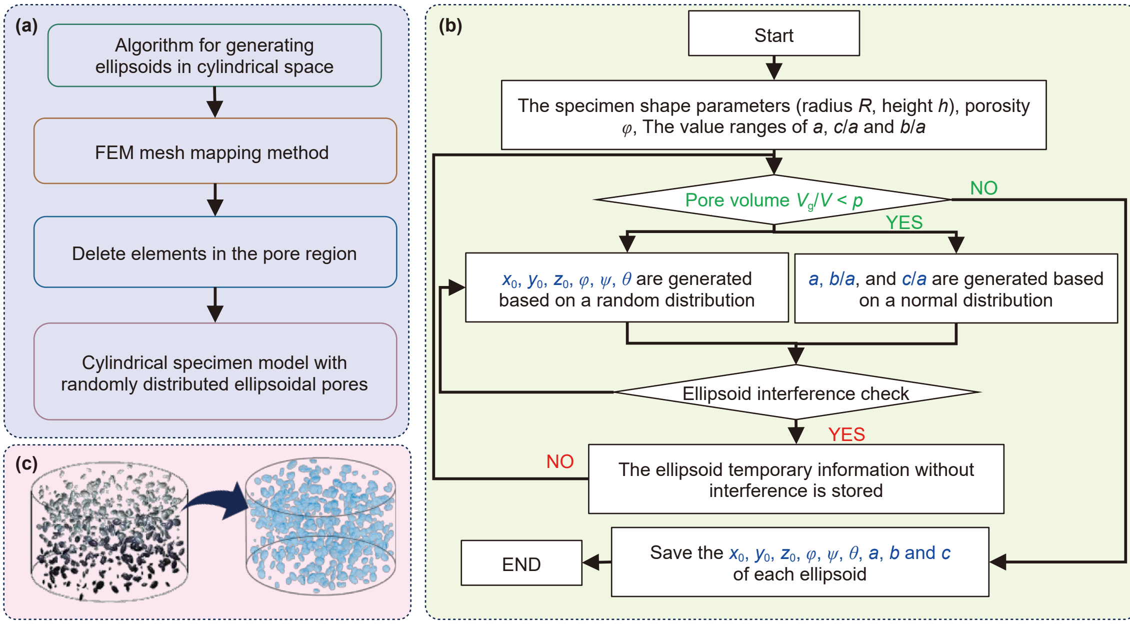

Fig. 2. The construction process of FEM model for porous specimens. (**a**) Construction process of cylindrical specimens with pores. (**b**) Algorithm for generating ellipsoids in cylindrical space. (**c**) Specimen models before and after meshing.

bar, while the remaining portion is reflected back into the incident bar (Zhang and Zhao, 2014).

Building on this operating principle, we developed a finite-element representation of the SHPB system as followed. The SHPB finite-element model (Fig. 4) explicitly represents a coaxial incident bar–porous rock specimen–transmission bar configuration in LS-DYNA and is solved using 3D explicit central-difference time integration. The incident bar has length $L_{In} = 5000$ mm and radius $R_{In} = 50$ mm; the cylindrical specimen has length $L_s = 50$ mm and radius $R = 50$ mm; the transmission bar has length $L_{Tr} = 3500$ mm and radius $R_{Tr} = 50$ mm. The two bars are modeled as linear-elastic solids with material constants (E_e, ν_e, ρ_e); the rock specimen contains randomly distributed ellipsoidal pores generated as described in Section 2 to match prescribed porosity and aspect-ratio statistics. All parts use 3D reduced-integration solid elements with *HOURGLASS control; the element size is selected according to the mesh-independence study in Section 3.3. Bar–specimen interfaces employ AUTOMATIC_SURFACE_TO_SURFACE contact with a Coulomb friction coefficient of $\mu = 0.3$. A half-sine axial pulse with reference period $T = 400$ μs is applied at the free end of the incident bar; trial analyses indicate a peak amplitude about 13 times the intrinsic rock strength, producing fragmentation over the porosity range 0–20%. The pulse parameters used here and in Section 4 are referenced to this baseline, and the amplitude ratios discussed in Section 5 are defined relative to the same baseline amplitude. The far end of the transmission bar is assigned a non-reflecting boundary to suppress end reflections. The time step is governed by *CONTROL_TIMESTEP under the CFL stability criterion (no mass scaling), and energy components together with hourglass energy are monitored to ensure numerical fidelity. Output is written via *DATABASE for full-field stress, strain, and damage; virtual strain-gauge nodes are placed at the midpoints of both bars to record strain histories, from which the normalized strength (σ_{norm}), energy dissipation density (U_v), and energy-dissipation ratio (η_U) are evaluated.

According to the fundamental principles of one-dimensional elastic wave theory, the stress $\sigma(t)$, the strain $\varepsilon(t)$ and the strain rate $\dot{\varepsilon}(t)$ of the specimen are time-dependent and determined by Eqs. (4)–(6), respectively (Kim and Changani, 2016; Li et al., 2018; Song et al., 2022; Du et al., 2023).

$$\sigma(t) = [\sigma_I(t) - \sigma_R(t) + \sigma_T(t)]A_e \,/\, (2A_s) \tag{4}$$

$$\varepsilon(t) = \int_0^t [\sigma_I(t) + \sigma_R(t) - \sigma_T(t)]\mathrm{d}t \Big/ \rho_e C_e L_s \tag{5}$$

$$\dot{\varepsilon}(t) = [\sigma_I(t) + \sigma_R(t) - \sigma_T(t)] \,/\, \rho_e C_e L_s \tag{6}$$

where, C_e is the wave velocity of the elastic wave in the bar, m/s; ρ_e is the density of the elastic bar, kg/m^3; L_s is the length of the specimens, m; $\sigma_I(t)$, $\sigma_R(t)$, $\sigma_T(t)$ represent the incident stress, reflected stress, and transmitted stress at a given time t, respectively, MPa; A_e, A_s represent the cross-sectional areas of the elastic bar and the specimen, respectively, m^2.

The normalized dynamic strength (σ_{norm}) was defined as Eq. (7), which could quantitatively characterize the impact dynamic strength of rocks with different pore structures.

$$\sigma_{norm} = \sigma_{d,pore} \Big/ \sigma_{d,in} \tag{7}$$

where, $\sigma_{d,pore}$ is the dynamic uniaxial strength of the porous specimen, MPa; $\sigma_{d,in}$ is the dynamic uniaxial strength of the non-porous specimen, MPa. The energy dissipation density (U_v) was defined to quantitatively characterize the energy dissipation efficiency during specimen failure, which can be calculated by:

$$U_v = U_s / V_s \tag{8}$$

where, V_s is the apparent volume of the specimen, m^3; U_s is the total energy dissipated during the specimen failure process, J, which can be calculated by:

$$U_s = U_I - U_R - U_T \tag{9}$$

where U_I, U_R, U_T are the incident energy, the reflected energy, and the transmitted energy. The calculation method for the relevant parameters is described in Stopka et al. (2024).

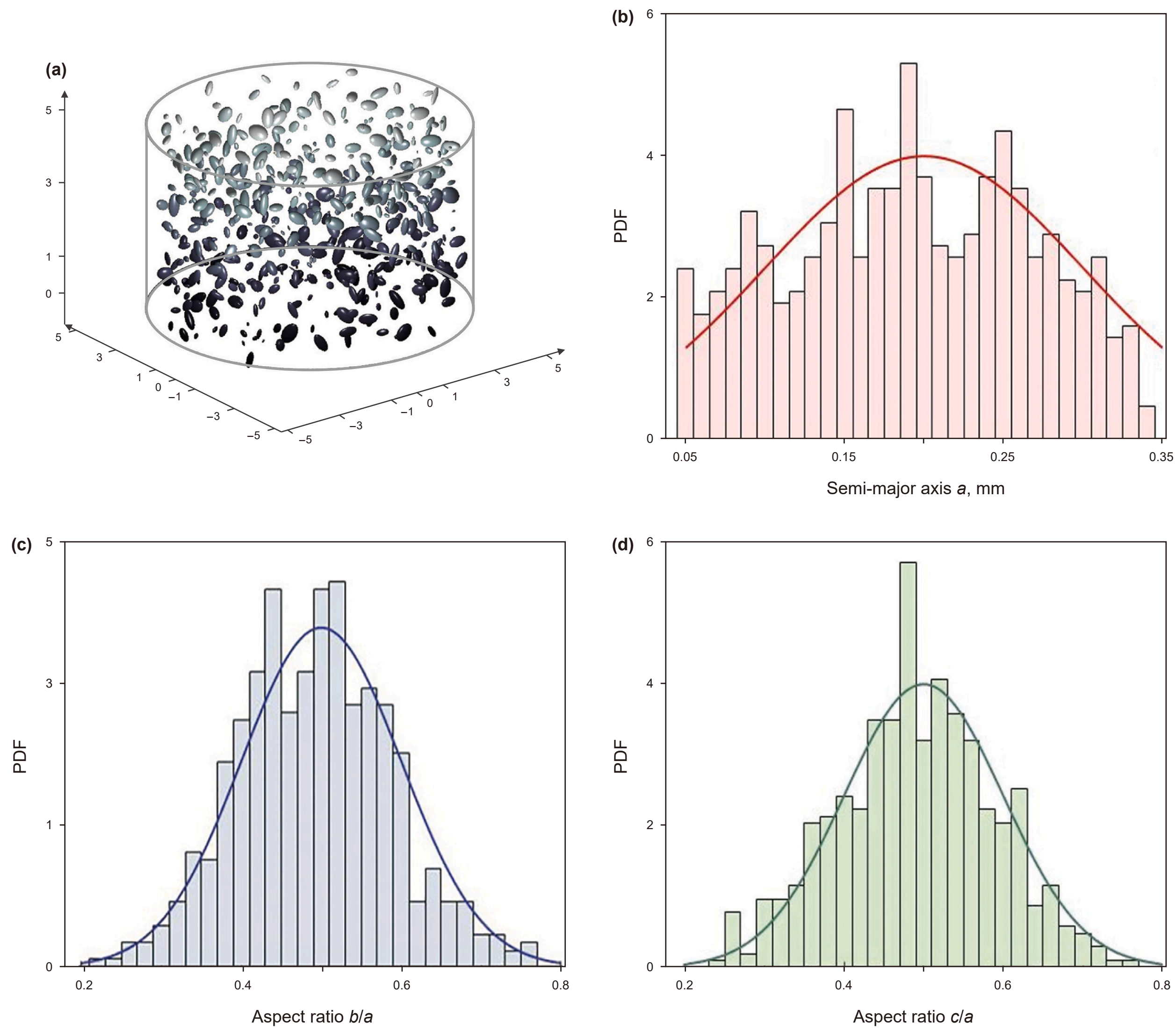

Fig. 3. Stochastic generation of ellipsoidal pores. (**a**) 3D cylindrical specimen with randomly distributed ellipsoidal pores. (**b**–**d**) Probability density functions (PDFs) of the sampled a, b/a, and c/a, respectively.

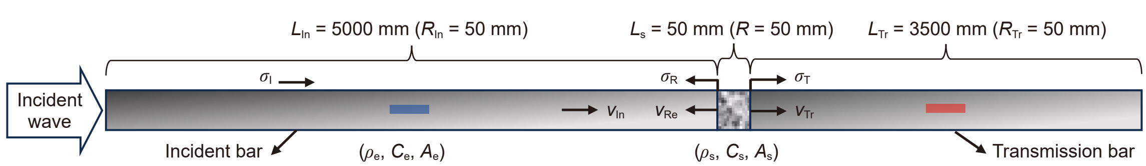

Fig. 4. Schematic diagram of the finite element model of the SHPB system (after Li et al., 2018).

3.2. Material parameter settings for the SHPB modelling

Based on the working principle of the SHPB, a FEM model of the SHPB system was constructed, with the geometric dimensions shown in Fig. 4. To simplify the model and accurately control the magnitude of the impact load, the striker bar was omitted, and the incident load was directly applied to the end face of the incident bar. A harmonic wave was used as the incident load. By recording the axial strain of elements located at the midpoints of the incident and transmission bars, the elastic waves in both bars can be obtained.

A linear elastic constitutive model was employed to describe the mechanical behavior of the bars, with a Young's modulus of 210 GPa, a Poisson's ratio of 0.2, and a density of 7.85 g/cm^3. For the rock specimen, the built-in RHT (Riedel-Hiermaier-Thoma) constitutive model in LS-DYNA was adopted. This model accounts for strain rate effects under moderate to high strain rate conditions and incorporates a comprehensive damage evolution mechanism. It captures the material's plastic deformation, tensile failure, and compressive failure characteristics, making it particularly well-suited for simulating damage accumulation under dynamic loading conditions. Xie et al. (2017) determined the RHT model parameters for granite through a series of uniaxial and triaxial experiments, achieving excellent agreement between the model predictions and experimental results. This parameter set has been validated in various impact and blasting simulations, demonstrating high stability and reliability. Therefore, the RHT parameter set listed in Table 1 is adopted in this study.

3.3. Validation of the FEM model

To ensure that the resluts of the SHPB numerical simulation accurately captures the mechanical behavior of materials under dynamic loading the stress equilibrium assessment, the mesh independence analysis, and reproducibility evaluation. As shown in Fig. 5(a), the superimposed waveform closely matches the trend of the transmission wave, indicating that the model satisfies the stress equilibrium condition. Fig. 5(b) presents the stress–strain curves of the specimen under different element sizes. It is observed that when the element size is smaller than 0.08 mm, the simulation results demonstrate good convergence. Therefore, an element size of 0.07 mm was selected in this study to balance computational accuracy and efficiency. Fig. 5(c) shows that the simulated dynamic stress–strain curve of granite agrees well with the experimental results reported by Yang S.Q. et al. (2023), confirming the reliability of the proposed model. Both the simulation and experiment exhibit similar linear responses during the elastic stage, with a simulated peak stress of approximately 160 MPa, which is close to the experimental value of about 170 MPa (the strength error is less than 7%). Distinct yielding and softening behaviors are observed in both cases. The simulated curve appears slightly smoother, mainly because the pore and crack distributions in the model are idealized and do not fully capture the stochastic nature of local failure.

To evaluate the reproducibility of the simulation results, five groups of specimen models were generated at porosity levels of 3%, 6%, and 9%, respectively, based on the pore structure parameters listed in Table 2. The dynamic compressive strength (σ_d), Young's modulus (E_d), and energy dissipation density (U_v) of these models were analyzed. As shown in Fig. 5(d), all three mechanical indicators exhibit a decreasing trend with increasing porosity. At porosity levels above 6%, the coefficients of variation (*CV*) are generally low, indicating good reproducibility. Specifically, the *CV* of σ_d and U_v remain within 0.2%–3%, while that of E_d is slightly higher, ranging from 3% to 8%, suggesting slightly lower consistency in stiffness measurements. Overall, specimens with higher porosity exhibit smaller fluctuations due to the larger number and more uniform distribution of pores. Extensive field measurements and laboratory tests indicate that the matrix porosity of carbonates typically falls within 3%–10% (Ng and Santamarina, 2023). Setting the study window at 6%–9% aligns well with this practical range and ensures numerical stability, thereby enabling a systematic elucidation of how pore geometry affects dynamic strength and energy metrics, and directly informing the optimization of impact loading parameters for drilling in carbonate formations.

Table 1
RHT constitutive model parameters of the specimen model (Xie et al., 2017).

Material parameters	Value
Density	2.66 g·cm^{-3}
Shear modulus	21.9 GPa
Parameter for polynomial EOS B_0	1.22
Parameter for polynomial EOS B_1	1.22
Parameter for polynomial EOS T_1	0.257
Parameter for polynomial EOS T_2	0
Failure surface parameter *A*	2.44
Failure surface parameter *N*	0.76
Compressive strength	167.8 MPa
Relative shear strength	0.21
Relative tensile strength	0.04
Lode angle dependence factor	0.68
Lode angle dependence factor	0.05
Compressive yield surface parameter	0.53
Tensile yield surface parameter	0.7
Hugoniot polynomial coefficient A_1	0.257
Hugoniot polynomial coefficient A_2	0.3784
Hugoniot polynomial coefficient A_3	0.2129
Residual surface parameter A_f	0.25
Residual surface parameter N_f	0.62
Break tensile strain rate	3.000e+19

4. Effect of pore parameters on dynamic mechanical behavior

In this study, four sets of numerical simulations (Groups A–D) were configured to isolate, respectively, the effects of porosity, pore size, pore aspect ratio, and pore orientation angle; this design enables a systematic single-parameter assessment, thereby quantifying each pore parameter's contribution to the dynamic mechanical response of rocks.

Group A simulations were designed to investigate the effect of porosity. Three representative pore shapes were considered—ellipsoidal, disk-shaped, and needle-shaped—corresponding to aspect ratio combinations of 0.75/0.75, 0.75/0.2, and 0.2/0.2, respectively. The prescribed porosity range for these pore geometries was set from 1% to 27% for ellipsoidal pores, 1% to 21% for disk-shaped pores, and 1% to 9% for needle-shaped pores.

Group B investigates pore-size effects by varying the major semi-axis *a*. On the one hand, matrix pores in carbonate rocks typically range from tens to hundreds of micrometers; thus $a = 0.15$ mm and $a = 0.45$ mm span a representative interval from large matrix pores to small macropores. On the other hand, the two sizes differ by a factor of three provides sufficient contrast to assess the sensitivity of σ_{norm}, U_v, and η_U to pore size. Therefore, $a = 0.45$ mm and $a = 0.15$ mm were selected as representative sizes. This setup may increase stochastic scatter, particularly for $a = 0.45$ mm where the pore count is lower; to enhance statistical robustness, five independent specimens were generated for each pore-size condition, and the arithmetic mean was used for comparison to mitigate randomness-induced bias. Group C focuses on the aspect ratio effect of ellipsoidal pores in three-dimensional space. To quantify pore geometry, this study introduces the sum of aspect ratios (S_{as}) and the difference of aspect ratios (D_{as}), defined by Eqs. (10) and (11). These two parameters jointly describe pore shape characteristics: S_{as} reflects the overall elongation of the two pores, while D_{as} captures the degree of asymmetry between them. When S_{as} is large and D_{as} is small, the pores tend to be similarly elongated and more elliptical, whereas a moderate S_{as} with a large D_{as} suggests that at least one pore is notably flatter, indicating greater shape anisotropy. Specifically, values of $b/a = 0.2$, 0.4, and 0.6 were defined, and for each case, c/a was gradually increased from the value of b/a to 0.8 to evaluate the influence of both aspect ratios on mechanical behavior. This design enables decoupled analysis of the bidirectional aspect ratio effects.

$$S_{as} = \frac{b}{a} + \frac{c}{a} \tag{10}$$

$$D_{as} = \left| \frac{b}{a} - \frac{c}{a} \right| \tag{11}$$

Group D examines the coupling effect between pore orientation angle and pore shape. Six different aspect ratio combinations were used. Among them, Groups D-1 to D-4 represent ellipsoidal and

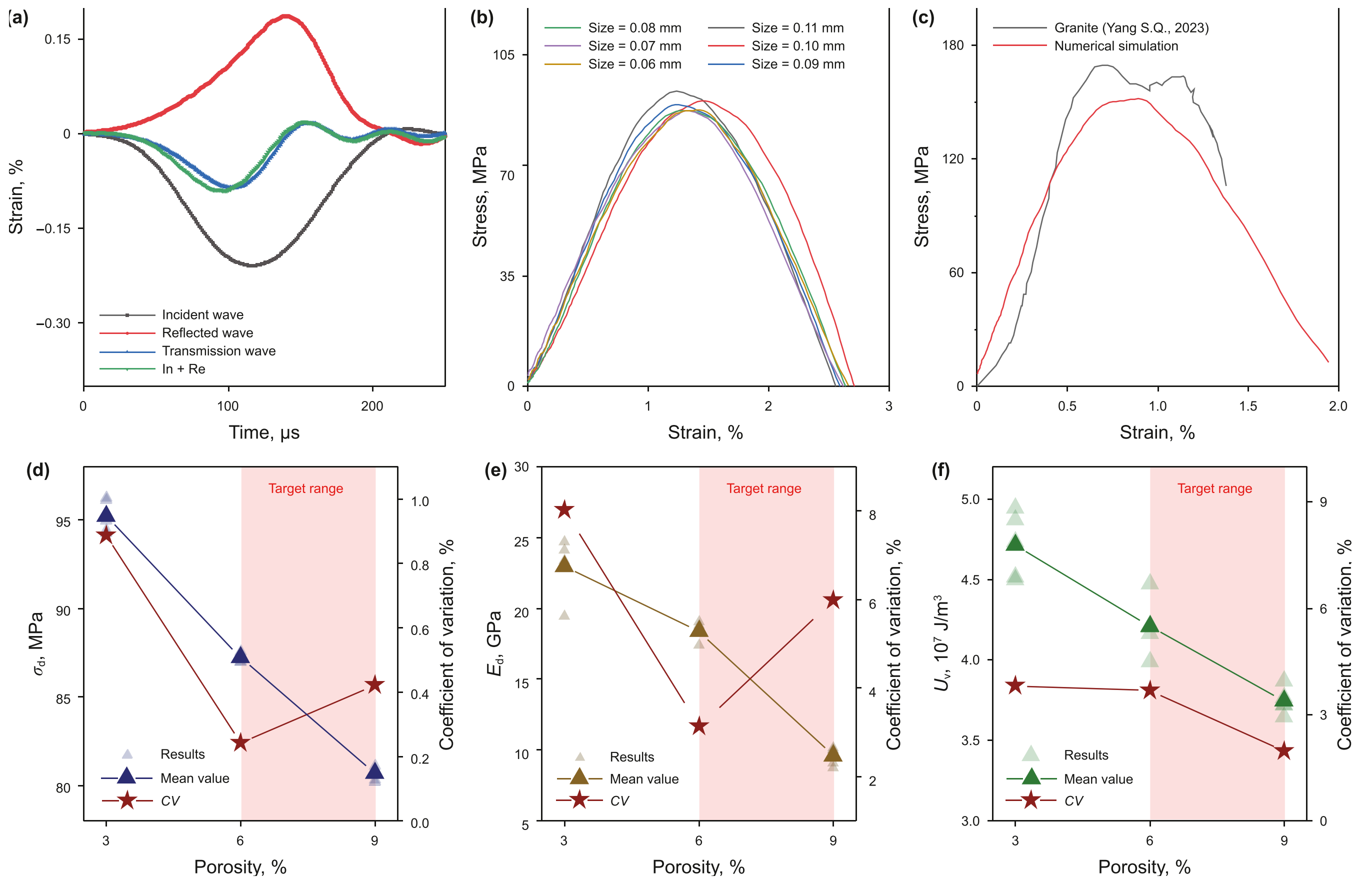

Fig. 5. Verification of the SHPB numerical model. (**a**) Stress balance verification. (**b**) Mesh-independence study for the specimen with 9% porosity using element sizes ranging from 0.06 to 0.11 mm. (**c**) Comparison between numerical simulation and experimental results (Yang S.Q. et al., 2023) for the dynamic response of granite. (**d**–**f**) Reproducibility of σ_d, E_d, U_v at 3%, 6%, and 9% porosities.

Table 2
Pore parameter setting for repeatability verification.

Parameter	Mean	Variance	Max.	Min.
a	0.25	0.1	0.35	0.15
(b/a)	0.75	0.1	0.9	0.6
(c/a)	0.75	0.1	0.9	0.6

needle-shaped pores with $b/a = c/a$, while Groups D-5 and D-6 correspond to disk-shaped pores with $b/a \neq c/a$. The pore orientation angle was varied from 0° to 90° to simulate the influence of the orientation of the pore's major axis relative to the loading direction on the mechanical response.

Table 3 provides detailed pore structure parameter settings for all simulation groups. Through this series of numerical simulations, the independent and coupled effects of porosity, pore size, pore shape, and orientation angle on the dynamic response of rocks were systematically investigated under conditions where pore structure parameters were carefully decoupled.

4.1. Effect of porosity on dynamic mechanical behavior

Fig. 6 illustrates the relationships between porosity and three key dynamic mechanical parameters—σ_{norm}, E_d and U_v—for rock specimens with three different pore shapes: ellipsoidal, disk-shaped, and needle-shaped. The results show that σ_{norm} decreases with increasing porosity across all pore types. This decline is more pronounced for specimens with ellipsoidal and disk-shaped pores, reaching approximately 0.75, whereas specimens with needle-shaped pores exhibit a relatively smaller reduction, stabilizing around 0.83. A similar trend is observed for E_d, with values decreasing from approximately 18 to 10–12 GPa in ellipsoidal and disk-shaped specimens, while the reduction is less significant in the presence of needle-shaped pores.

Fig. 6(c) shows that U_v decreases with increasing porosity for specimens with all pore shapes, although the rate of decrease varies depending on poreshape. Specimens with ellipsoidal and disk-shaped pores exhibit a relatively smooth decline in U_v, whereas those with needle-shaped pores show a more pronounced reduction. This may be attributed to the enhanced connectivity between fractures along short paths in high-porosity specimens with needle-shaped pores, which reduces the energy required for crack propagation and thus significantly lowers U_v. Although the number of ellipsoidal pores is smaller than that of disk-shaped pores, their U_v values remain consistently lower, suggesting that the fracture evolution process is governed not only by pore shape but also by other microscale factors.

Overall, the increase in porosity reduces the compressive strength, stiffness, and energy dissipation during failure in rocks. Among the different pore shapes, increases in the porosity of ellipsoidal and disk-shaped pores have a more pronounced effect on strength and elastic modulus, whereas increases in the porosity of needle-shaped pores have a more significant impact on the energy dissipated during failure.

Fig. 7 illustrates the distinct differences in damage evolution among ellipsoidal pore specimens with porosities of 0.73%, 4.60%,

Table 3
Pore parameter setting of each group of specimens.

Decoupling parameters	Group	Pore parameters				
		φ_0, %	a, mm	b/a	c/a	θ, °
Porosity	A1	[1: 2: 27] *1	0.25 (0.2, 0.3) *2	0.75 (0.6, 0.9)	0.75 (0.6, 0.9)	U (0°, 180°)*3
	A2	[1: 2: 27]	0.25 (0.2, 0.3)	0.75 (0.6, 0.9)	0.2 (0.15, 0.25)	U (0°, 180°)
	A3	[1: 2: 27]	0.25 (0.2, 0.3)	0.2 (0.15, 0.25)	0.2 (0.15, 0.25)	U (0°, 180°)
Pore size	B1	9	0.15, 0.45	0.5 (0.2, 0.8)	0.5 (0.2, 0.8)	U (0°, 180°)
Aspect ratio	C1	6	0.25 (0.2, 0.3)	0.2	0.2, 0.4, 0.6, 0.8	U (0°, 180°)
	C2	6	0.25 (0.2, 0.3)	0.4	0.4, 0.6, 0.8	U (0°, 180°)
	C3	6	0.25 (0.2, 0.3)	0.6	0.6, 0.8	U (0°, 180°)
Orientation	D1	8	0.25 (0.2, 0.3)	0.2 (0.15, 0.25)	0.2 (0.15, 0.25)	[0°: 15°: 90°]
	D2	8	0.25 (0.2, 0.3)	0.4 (0.35, 0.45)	0.4 (0.35, 0.45)	[0°: 15°: 90°]
	D3	8	0.25 (0.2, 0.3)	0.6 (0.55, 0.65)	0.6 (0.55, 0.65)	[0°: 15°: 90°]
	D4	8	0.25 (0.2, 0.3)	0.8 (0.75, 0.85)	0.8 (0.75, 0.85)	[0°: 15°: 90°]
	D5	8	0.25 (0.2, 0.3)	0.2 (0.15, 0.25)	0.8 (0.75, 0.85)	[0°: 15°: 90°]
	D6	8	0.25 (0.2, 0.3)	0.4 (0.35, 0.45)	0.6 (0.55, 0.65)	[0°: 15°: 90°]

*1 Parameters in [min: step: max] specify the range: minimum, increment, and maximum.
*2 Parameters in μ (max, min) specify an ecologically distributed random variable: mean, maximum, and minimum, with variance fixed at 0.1 in this study.
*3 'U (0°, 180°)' denotes the uniform random distribution of θ over the interval of 0° to 180°.

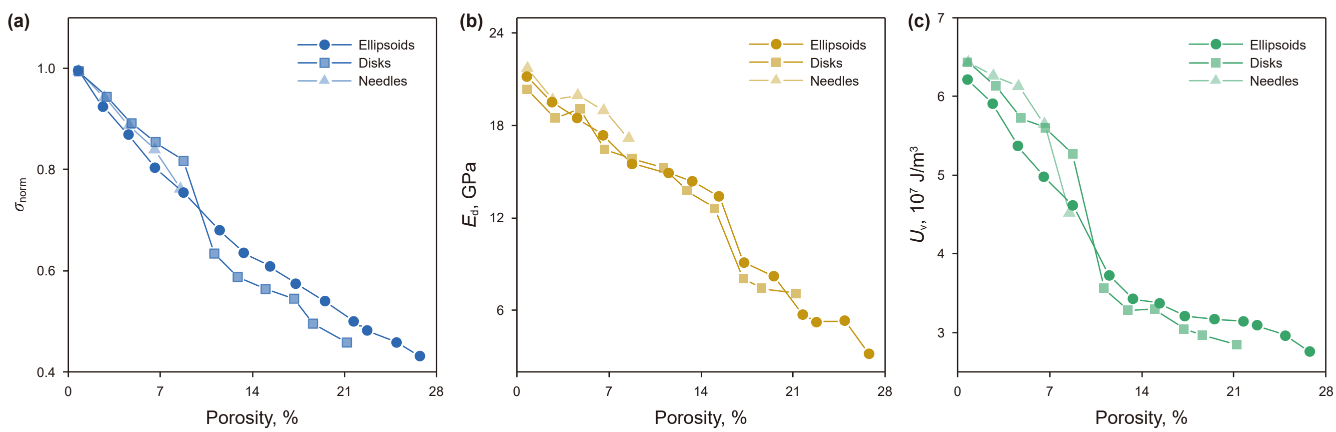

Fig. 6. Porosity effects for different pore shapes under dynamic loading. (**a**–**c**) σ_{norm}, E_d, U_v for specimens with ellipsoidal, disk-shaped, and needle-shaped pores, respectively.

and 8.26% under identical impact loading. At the early stage of impact (1000 μs), damage first initiates at the pore edges and propagates along the loading direction. The selection of 1000 μs as the early-stage time point corresponds approximately to the arrival time of the incident stress wave at the specimen, which can be estimated by $t_{In} = L_{In}/\sqrt{E_{In}/\rho_{In}} \approx 968$ μs, where $L_{In} = 5$ m is the length of the incident bar. E_{In} and ρ_{In} are the Young's modulus and the density of the incident bar, respectively, which were shown in Section 3.3. This confirms that 1000 μs effectively captures the onset of stress transfer from the bar to the specimen. Additionally, the damage distribution outside the pore regions is non-uniform, with more severe damage observed near the specimen end faces. This indicates that under high loading rates, stress transmission along the specimen axis is uneven.

As the stress wave propagates (1040 μs), the damage extent in the low-porosity specimen is relatively limited, and does not develop into a large-scale failure zone. In contrast, the high-porosity specimen exhibits increasingly interconnected internal damage, forming a pronounced damage band near the specimen end face. The thickness of this damage band increases with porosity, indicating a reduction in load-bearing capacity in the end regions. This phenomenon explains the observed decrease in E_d with increasing porosity shown in Fig. 6(b). Moreover, the overall intensification of damage provides a mechanistic explanation for the reduction in specimen strength with increasing porosity, as presented in Fig. 6(a).

At the late stage of impact loading (1070 μs), all specimens exhibit macroscopic failure characteristics. The specimen with 1% porosity primarily develops axial and transverse cracks, which remain relatively isolated from each other. In the 5% porosity specimen, inclined cracks begin to appear, whereas the 9% porosity specimen develops a dense and irregular network of interconnected cracks. The evolution of crack morphology indicates that, under low-porosity conditions, fractures tend to remain confined to local regions around isolated pores. In contrast, high-porosity specimens more readily facilitate crack coalescence between adjacent pores, leading to the formation of a continuous macroscopic failure network. This finding is consistent with the results reported by Sun et al. (2025). It is worth noting that the pores constructed in Section 2.1 are entirely isolated internal structures that do not intersect with the specimen's external boundaries. Therefore, for cracks to be observed on the specimen surface, they must evolve progressively from internal damage zones toward the exterior. In other words, the visible surface cracks can be regarded as the external manifestation of internal damage evolution induced by pore interactions. In high-porosity specimens, the increased density of internal pores enhances the likelihood of crack bridging between neighboring voids, eventually

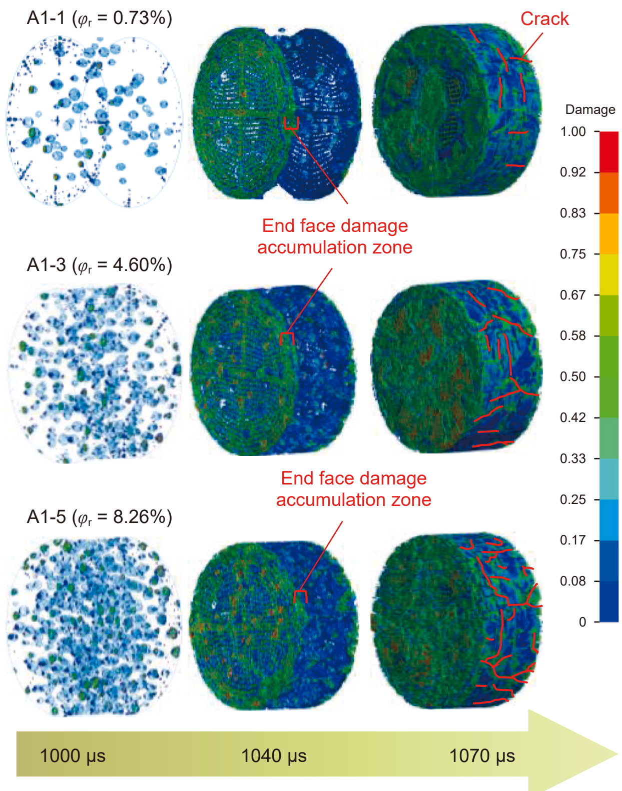

Fig. 7. Damage evolution of specimens with different porosities.

forming a more connected fracture network with lower complexity of crack paths. As crack paths become shorter and propagation resistance diminishes, the connectivity of damage zones is significantly improved. This reduction in crack development and extension energy explains the decreasing trend of U_v with increasing porosity, as observed in Fig. 6(c).

4.2. Effect of pore size on dynamic mechanical behavior

Fig. 8 illustrates the influence of pore size on the dynamic mechanical behavior of rocks. It is observed that as the pore size

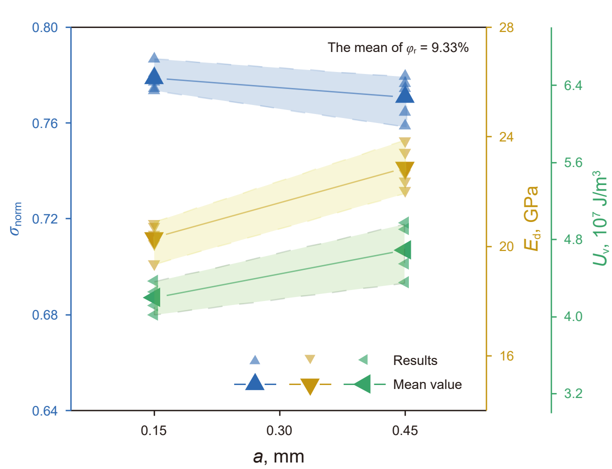

Fig. 8. Effect of pore size on mechanical response and energy dissipation of specimens. Normalized peak stress σ_{norm}, dynamic Young's modulus E_d, and energy dissipation density U_v versus a.

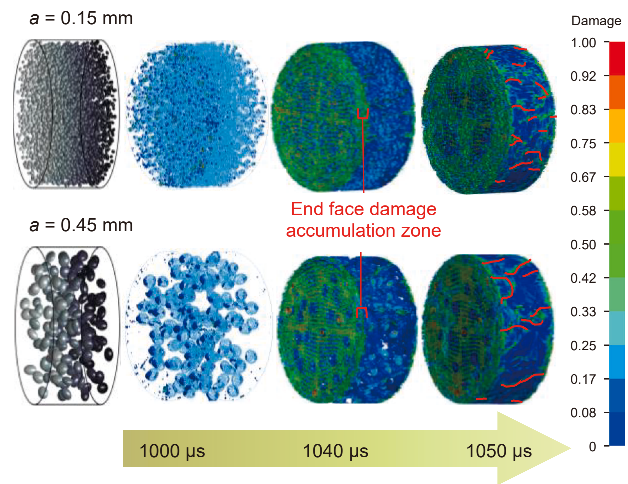

Fig. 9. Damage evolution of specimens with different pore sizes.

increases, σ_{norm} of the specimens decreases significantly. Specimens with smaller pores exhibit higher impact resistance, whereas those with larger pores demonstrate considerably reduced load-bearing capacity. This suggests that larger pores weaken the overall structural integrity of the material under impact loading. These findings stand in marked contrast to the numerical simulations under quasi-static conditions reported by Fakhimi and Gharahbagh (2011), which suggested that, at a constant porosity, specimens with larger pores tend to exhibit higher macroscopic Young's modulus and compressive strength, as well as greater variability in mechanical properties.

This discrepancy arises primarily from the fundamentally different loading modes and dominant failure mechanisms. Under quasi-static loading, failure is mainly governed by tensile crack propagation, where larger pores contribute to a more robust load-bearing skeleton that delays crack growth and enhances macroscopic strength. In contrast, under the high-strain-rate impact simulations conducted in this study, failure is more strongly influenced by localized strain-rate-driven crushing and shear mechanisms, with stress concentrations around the pores becoming a critical factor. This distinction is further supported by the damage evolution process shown in Fig. 9.

In the initial loading stage (1000 μs), damage initiates around the pore edges in all specimens, with the large-pore specimens exhibiting a more extensive initial damage zone, indicating more severe localized stress concentrations. Notably, during SHPB impact loading, end-face regions often experience early damage accumulation due to the combined effects of rapid stress wave rise time, frictional constraints, and wave impedance mismatch, leading to what is known as the “end effect” (Hao et al., 2013; Yang Y. et al., 2023). This effect increases the non-uniformity of damage distribution and significantly affects subsequent wave reflection, stress trapping, and stiffness responses.

As the stress wave propagates through the specimen (1040 μs), the small-pore specimens develop thick damage accumulation zones near the top and bottom ends. In contrast, large-pore specimens, due to their relatively sparse end-face pore structure, experience more constrained deformation in these regions, resulting in narrower damage bands. These end-face structural differences significantly influence wave reflection behavior. The dense pore distribution at the ends of small-pore specimens promotes local wave overlapping and stress retention, leading to higher E_d, whereas the stiffness of large-pore specimens remains relatively low.

In the later stage (1050 μs), the densely distributed pores in small-pore specimens facilitate multiple pathways for crack initiation and coalescence, resulting in shorter crack propagation paths, faster fracture penetration, and lower U_v. Conversely, the crack paths in large-pore specimens are longer and more tortuous, resulting in higher fracture resistance and greater energy dissipation, despite fewer total cracks.

4.3. Effect of pore aspect ratio on dynamic mechanical behavior

Fig. 10 illustrates the influence of different pore aspect ratio combinations on the dynamic mechanical properties of rock specimens. The results indicate that σ_{norm} decreases significantly with increasing D_{as}, suggesting that the flatter the pore shape, the more pronounced its weakening effect on rock strength. This trend is consistently observed both within groups (e.g., in Group C1, σ_{norm} decreases from 0.815 to 0.78) and across groups (e.g., comparisons among C3-2, C2-3, and C1-4), revealing that D_{as} plays a more critical role in determining rock strength than their absolute values. Previous relative study (Griffiths et al., 2017) based on two-dimensional models have demonstrated that variations in pore aspect ratio can alter the distribution of stress concentration and the fracture propagation path, thereby affecting the strength, elastic modulus, and damage evolution behavior of rocks. However, these studies neglect the synergistic influence between two distinct aspect ratios of pores in three-dimensional space, which may play a critical role in modulating mechanical responses. This finding addresses the limitations of two-dimensional models that consider only a single aspect ratio and further explains the more significant strength reduction observed in disk-shaped pore specimens, as discussed in Section 4.1.

In contrast to strength, E_d generally exhibits an increasing trend with the growing difference between the two aspect ratios. This pattern is particularly evident in Groups C1 and C3. However, Group C2 and several individual specimens (e.g., C1-4, C3-2, and C2-3) show certain fluctuations, which may be attributed to the relatively high coefficient of variation in the simulation of E_d.

Fig. 10(c) presents the effect of aspect ratio difference on U_v. Overall, U_v increases with increasing aspect ratio difference—for example, in Group C1, U_v rises from 4.3×10^7 to 5.1×10^7 J/m^3. This trend is primarily attributed to the fact that, under constant porosity, reducing the aspect ratio in one direction decreases the volume of individual pores while increasing their number and spatial density. As a result, crack propagation paths are shortened and energy dissipation is enhanced. However, in specimens with $b/a = 0.2$ (e.g., C1-2 and C1-3), U_v shows an abnormal increase, suggesting that disk-shaped pores may induce more complex crack networks, thereby leading to higher energy dissipation.

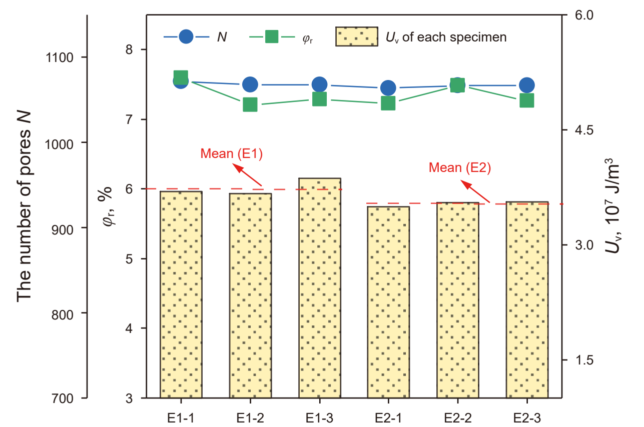

Fig. 11. The effect of pore shape on U_v. Solid bars show U_v of individual specimens E1-1 to E2-3 (right axis). Overlaid curves report the pore count N and the porosity φ_r for each specimen.

To verify the hypothesis that disk-shaped pores can lead to an increase in U_v, a series of numerical simulations was conducted, referred to as Group E. To eliminate the influence of differences in porosity and pore number on the results, the specimens in Group E were designed to ensure approximately consistency in actual porosity and pore count between the two pore types—disk-shaped and ellipsoidal pores. The specific procedure was as follows: a disk-shaped pore specimen ($b/a = 0.8$, $c/a = 0.2$) was first constructed with a prescribed porosity of 7%. After mesh generation, φ_r of the disk-shaped pore specimen is approximately 7.5%, with the number of pores ranging from 1044 to 1076, as illustrated in Fig. 11. When both the porosity and pore number of the ellipsoidal-pore specimen are simultaneously higher or lower than those of the disk-shaped specimen, the prescribed porosity is adjusted accordingly. Following this adjustment, two scenarios may occur: (1) If the porosity reaches or exceeds that of the disk-shaped specimen but the number of pores remains lower, the pore aspect ratio of the ellipsoidal pores is slightly decreased. (2) Conversely, if the number of pores reaches or exceeds that of the disk-shaped specimen but the porosity remains lower, the pore aspect ratio is increased. This iterative process is repeated until the actual porosity and pore count of the ellipsoidal-pore specimen become approximately equal to those of the disk-shaped specimen. The final parameters selected were $b/a = c/a = 0.54$ with a

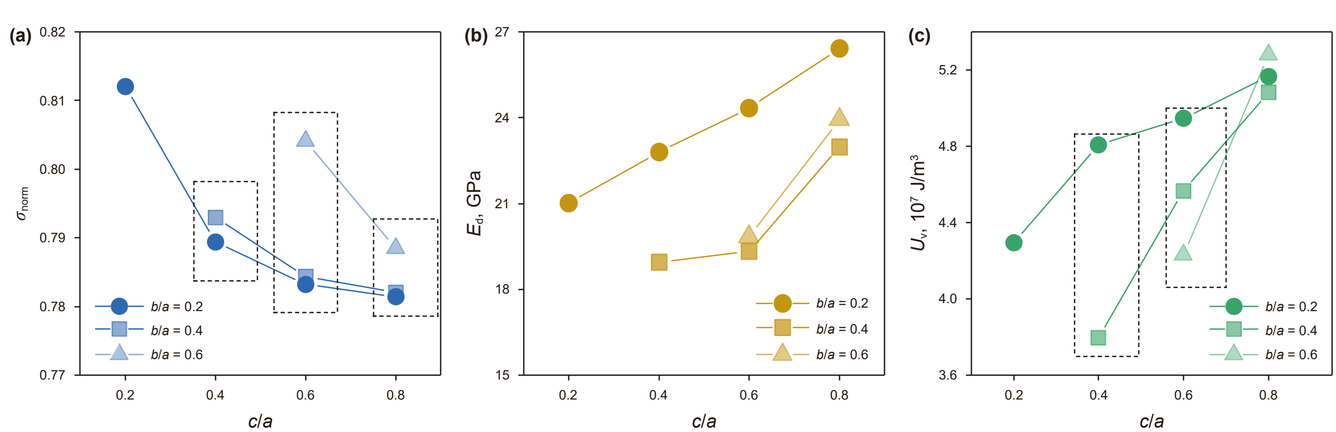

Fig. 10. Effect of pore aspect ratios on mechanical response and energy dissipation. (**a**) σ_{norm}; (**b**) E_d; (**c**) U_v versus c/a for $b/a = 0.2, 0.4, 0.6$.

prescribed porosity of 5.85%, under which the actual porosity and pore count matched those of the disk-shaped specimen. Three specimens were generated for each pore type (E1-1, E1-2, and E1-3 for disk-shaped pores; E2-1, E2-2, and E2-3 for ellipsoidal pores).

Fig. 11 presents the actual porosity (φ_r), pore number (N), and corresponding U_v values for all six specimens, along with a comparison of the average U_v between the two groups. The results indicate that, under identical porosity and pore number conditions, the average U_v of the disk-shaped pore specimens is 3.74×10^7 J/m^3, which is approximately 6% higher than that of the ellipsoidal pore specimens (3.53×10^7 J/m^3). This result confirms that disk-shaped pore structures lead to higher energy dissipation during dynamic failure.

Fig. 12 illustrates the damage evolution at various stages of impact loading for specimens with different pore aspect ratios. At the early stage of impact (1000 μs), the end-face damage in specimen C1-1 is more densely distributed, whereas it is relatively sparse in specimen C1-4. This is because a higher aspect ratio (as in C1-4) corresponds to larger individual pore volumes and fewer total pores, resulting in a lower pore density near the end face. Consequently, there are fewer stress concentration points and fewer initial damage zones. Therefore, specimen C1-1 is more prone to developing widespread initial damage.

As the stress wave propagates (1040 μs), the damage accumulation layer at the end face of C1-4 thickens significantly, further confirming its inferior structural capacity. These observations demonstrate that an increase in the difference between pore aspect ratios leads to a reduction in overall specimen strength, which is consistent with the trend shown in Fig. 10(a), where strength decreases with increasing aspect ratio difference.

At the later stage of impact (1060 μs), the complexity of crack paths within specimen C1-4 is noticeably larger than that of C1-1, with more densely developed surface cracks. In specimen C1-1, cracks primarily propagate along the axial direction, with occasional oblique connections. In contrast, specimen C1-4 exhibits a complex crack network composed of interwoven axial and circumferential fractures. Although C1-4 contains fewer pores, cracks are more likely to coalesce between pores, forming a more intricate fracture network and thereby enhancing energy dissipation. This suggests that disk-shaped pores are more prone to triggering complex crack systems during failure, leading to greater energy consumption. This observation explains the increasing trend of U_v with aspect ratio difference observed in specimens from both Groups C1 and E1.

4.4. Effect of pore orientation angle on dynamic mechanical behavior

The angle between the loading direction and the plane formed by the pore's major and minor axes is defined as the pore orientation angle (θ) (refer to the schematic diagram on the right side of Fig. 13). Fig. 13 shows the variation in σ_{norm} with θ under different pore aspect ratios. As shown in Fig. 13, σ_{norm} generally decreases with increasing θ, and the trends differ depending on the aspect ratio configuration. When $b/a = c/a$, the variation of σ_{norm} is relatively small. Moreover, the larger the aspect ratio, the weaker the influence of θ on σ_{norm}, indicating a reduced stress concentration response. For example, when $b/a = 0.8$, σ_{norm} remains nearly constant with increasing θ, suggesting that under high aspect ratio conditions, the effect of θ on σ_{norm} is minimal.

In contrast, when $b/a \neq c/a$, the effect of θ on σ_{norm} becomes more pronounced. As illustrated by the purple and yellow curves, σ_{norm} decreases significantly from approximately 0.84 to 0.5 as θ increases from 0° to 90°. Notably, at $\theta = 0°$, specimens D5-1 and D6-1 exhibit higher σ_{norm} compared to those in Groups D2–D4; however, their strength declines rapidly with increasing θ. This indicates that while disk-shaped pore specimens possess higher load-bearing capacity at small orientation angles, they are more sensitive to variations in θ. In summary, θ influences the strength by regulating the degree of local stress concentration, and its effect is strongly dependent on pore geometry: disk-shaped pores exhibit higher sensitivity to θ, whereas pores with high aspect ratios are less affected.

Fig. 14 illustrates the effect of different θ on the damage evolution process of rock specimens under impact loading, under conditions of high aspect ratio difference ($b/a = 0.8$, $c/a = 0.2$). At the early stage of impact (1000 μs), initial damage in all specimens is concentrated around pores near the specimen end face. For specimens with small orientation angles, damage is primarily confined to the tips of the disk-shaped pores and remains limited in extent. However, as θ increases to 60° and above, distinct agglomerate damage zones begin to develop around the pores. By 1040 μs, damage in low θ specimens remains relatively sparse and extends mainly along the loading direction, while high θ specimens exhibit a denser, interwoven network of axial and transverse damage structures. This evolution indicates that under high pore

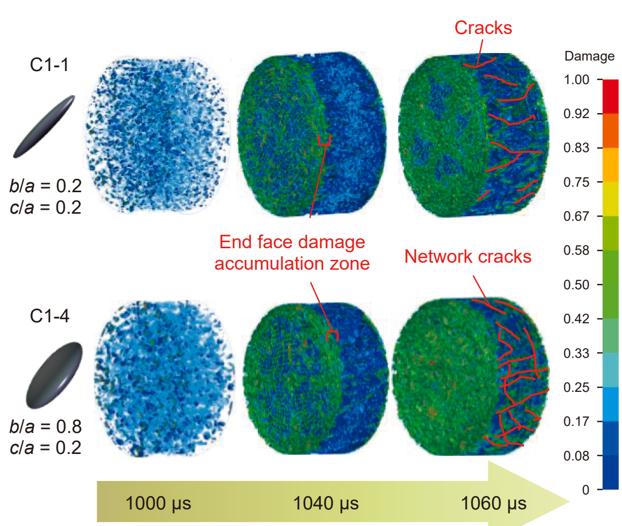

Fig. 12. Damage evolution of specimens with different aspect ratios.

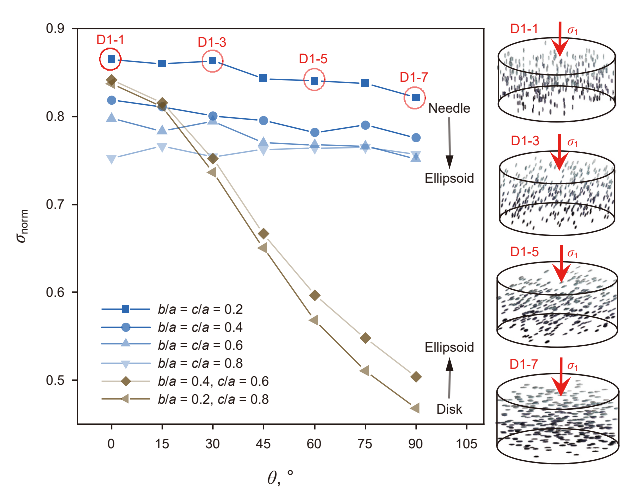

Fig. 13. Effect of θ on mechanical response of specimens.

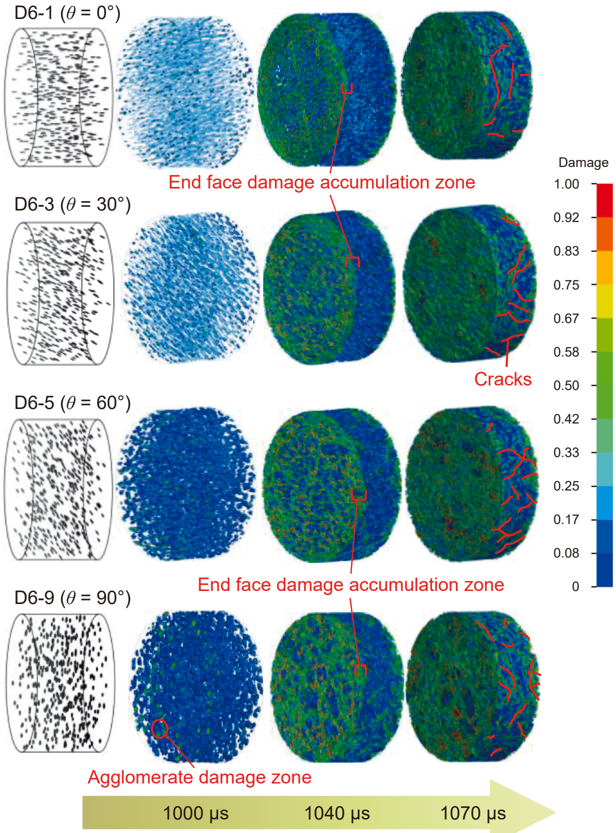

Fig. 14. Damage evolution of specimens with different θ.

aspect ratio conditions, low θ pores maintain stronger stress-bearing capacity. In contrast, increasing θ significantly weakens the surrounding material, facilitating damage initiation and accumulation, which ultimately leads to a reduction in strength.

At the later stage of impact (1070 μs), pronounced macroscopic cracks develop in the specimens, with crack shape exhibiting distinct characteristics depending on θ. At $\theta = 0^\circ$, cracks propagate along both the loading direction and its perpendicular direction. At $\theta = 30^\circ$ and 60°, inclined through-cracks appear and increase in length. At $\theta = 90^\circ$, cracks become denser but are primarily composed of short, oblique fractures. These results indicate that pore orientation angle significantly influences the rock's fracture mode under impact loading. Specifically, high-orientation pores are more likely to trigger multidirectional cracking, thereby compromising the overall structural integrity of the rock mass.

4.5. Correlation analysis of pore structure parameters with dynamic mechanical responses

In order to quantitatively characterize the influence of factors such as porosity, pore size, pore distribution density, and pore aspect ratio on the rock mechanical properties, a correlation analysis was conducted between the various pore parameters and the rock dynamic mechanical parameters. It is important to note that the results of the D-group numerical simulations show a strong correlation between σ_{norm} and θ, while no significant correlation was observed between U_v or E_d and θ. To minimize the interference of the D-group results on the correlation analysis, the pore orientation angle was excluded from the analysis, and the dataset was constructed based solely on the numerical simulation results from the A, B, C, and E groups, with θ randomly distributed.

It is worth emphasizing that although θ was not explicitly included in the correlation analysis, it still exerts a notable influence on the dynamic mechanical response of rocks. As illustrated in Fig. 13, θ exhibits a coupled relationship with pore shape. When pores become more flattened, local stress concentration intensifies, thereby amplifying the sensitivity of rock strength to pore orientation.

In constructing the dataset, φ_r was used to represent the specimen's porosity, the semi-major axis length a was used to represent the pore size, and pore count N was used to represent the specimen's pore distribution density. The sum of pore aspect ratios (S_{as}) and the difference of pore aspect ratios (D_{as}) were used to characterize the pore aspect ratio. For variables assumed to follow a normal distribution, only the mean was considered, and the differences in maximum values, minimum values, and variance were neglected.

Based on the dataset, the Pearson correlation coefficient, Spearman correlation coefficient, and Kendall correlation coefficient were calculated to assess the relationships between porosity (φ_r), pore size (a), pore count (N), and the pore aspect ratio parameters (S_{as} and D_{as}) with σ_{norm}, E_d, and U_v. Fig. 15 presents the results of the correlation analysis. In all three figures, the correlation coefficients for φ_r are the largest, indicating that porosity has the most significant influence on the three dynamic mechanical parameters. The absolute values of the correlation coefficients for σ_{norm} and U_v are both greater than 0.7, suggesting a strong correlation between σ_{norm} and U_v with porosity. This result aligns with static mechanical studies, which show that porosity is the most significant pore parameter influencing rock mechanics.

From Fig. 15(a), it can be observed that all five pore parameters exhibit a negative correlation with σ_{norm}, consistent with previous numerical simulation results. Apart from porosity, a and D_{as} have relatively large correlation coefficients with absolute values close to 0.4, indicating that pore size and the difference in pore aspect ratios significantly influence specimen strength. Among these, D_{as} represents the flattening degree of pores, meaning that the larger D_{as} is, the flatter the pores become. The correlation coefficient for D_{as} is greater than that for S_{as}, indicating that changes in the difference in pore aspect ratios have a more significant effect on specimen strength compared to changes in pore aspect ratios. This also suggests that flattened pores have a more pronounced weakening effect on rock strength.

From Fig. 15(b), it can be seen that, apart from porosity, both a and N exhibit a positive correlation with E_d, with the correlation result for a being consistent with the findings in Fig. 8. It should be noted that both increased a and decreased porosity lead to a reduction in N, so in this case, N and E_d should exhibit a negative correlation, which contradicts the result shown in Fig. 15(b). The reason for this contradiction could be the high randomness of the E_d simulation results. The large coefficient of variation in the E_d values in Fig. 5(b) may explain this discrepancy.

Fig. 15(c) showed that, apart from porosity, a and D_{as} exhibit a negative correlation with U_v, while N and S_{as} show a positive correlation with U_v. Notably, the absolute values of the correlation coefficients for a, U_v, and S_{as} are all less than 0.3, indicating a relatively weak correlation between these three factors and U_v. In contrast, D_{as} shows a stronger correlation, which to some extent validates the conclusion that more flattened pores lead to a larger U_v.

5. Dynamic mechanical response of specimens under the coupled influence of pore structure and impact parameters

The mechanical responses of specimens with different pore structure parameters were systematically investigated under

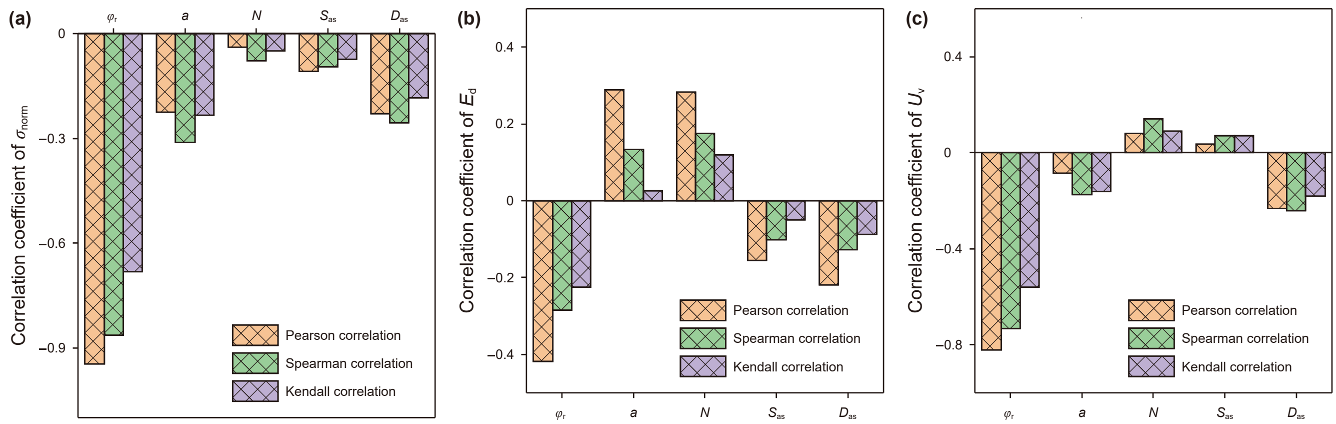

Fig. 15. Correlation between mechanical indices and pore-structure parameters. Bar heights give Pearson, Spearman, and Kendall coefficients. (**a**) σ_{norm}; (**b**) E_d; (**c**) U_v versus pore parameters: φ_r, a, N, S_{as}, and D_{as}.

impact stress waves of varying amplitude and period. For convenient comparison and quantitative analysis of stress wave amplitudes under different loading conditions, the normalized impact stress wave amplitude (A_{norm}) is defined in this study as the ratio of the stress wave amplitude (σ_{impact}) to the uniaxial compressive strength ($\sigma_{d,in}$) of the matrix of porous rock specimens, i.e., $A_{norm} = \frac{\sigma_{impact}}{\sigma_{d,in}}$. The wave periods were defined as 200 μs (5000 Hz, high-frequency impact), 400 μs (2500 Hz, medium-frequency impact), and 800 μs (1250 Hz, also medium-frequency impact), with 400 μs being the reference period used in prior simulations. In this study, the characteristic frequency of the incident impact wave denotes the frequency intrinsic to a single impact waveform, determined by its temporal features (e.g., impact period and rise time), whereas the operating frequency of a rotary-percussive downhole tool in drilling is the number of repeated impacts per unit time, corresponding to an intermittent sequence of impacts; the two are conceptually and operationally distinct. Systematically examining specimen responses across different incident-wave characteristic frequencies elucidates how the loading time structure governs strength, damage evolution, and energy utilization, and provides quantitative guidance for optimizing pulse width and striking rhythm in impact drilling, thereby improving rock-breaking efficiency.

Since U_v typically increases with the incident wave energy, comparisons across different loading amplitudes or specimen volumes may obscure differences in energy-use efficiency. To address this, the energy-dissipation ratio was defined as η_U, which quantifies the fraction of incident energy consumed by irreversible damage and fracture. During drilling operations, a higher η_U indicates that more impact work is converted into crack propagation and cuttings generation rather than elastic rebound, reflection, or radiative losses, thereby better reflecting rock-breaking efficiency; this is consistent with the field concept of mechanical specific energy (η_U) be calculated by:

$$\eta_U = U_v/W_{In} \times 100\% \tag{12}$$

where W_{In} represents the incident wave energy. In the present numerical simulation, stress is directly applied to the end face of the incident bar. Under this loading method, the incident energy is equal to the energy carried by the incident wave within the incident bar. Eq. (12) is adopted as Eq. (13) in this study.

$$\eta_U = U_v/U_I \times 100\% \tag{13}$$

Based on the findings presented in Section 4, porosity, pore size, and pore shape exert significant influences on the strength and energy dissipation behavior of rocks. Therefore, this chapter further investigates the effects of these three pore parameters on the mechanical response of rocks under different impact wave periods and stress wave amplitudes. The analysis is conducted using the specimen models developed in Section 3. To investigate different influencing factors on rock mechanical behavior, three specimens from Group A1 are selected to assess the effect of porosity; three specimens each from Groups B1 and B2 are used to evaluate the impact of pore size; and specimens from Groups E1 and E2 are utilized to study the effect of pore shape. A comprehensive summary of the parameter configurations is provided in Table 4.

5.1. Dynamic mechanical response of specimens under the coupled influence of pore structure and impact stress wave period

As shown in Fig. 16(a), for specimens at all porosity levels, σ_{norm} reaches its maximum at $T = 400$ μs; this rule likewise holds for different pore sizes (Fig. 16(b)) and different pore shapes (Fig. 16(c)). U_v increases with T, and the difference in U_v among periods is largest at a porosity of around 5%, where the maximum U_v exceeds about 3.5×10^7 J/cm^3. This indicates that at 5% porosity the sensitivity of U_v to T is the strongest, whereas this sensitivity decreases markedly when $\varphi_r > 5\%$. The optimum and trend of η_U with respect to T are also porosity-dependent: when $\varphi_r < 5\%$, η_U shows a slow overall increase with T; as porosity increases, the period corresponding to the peak η_U gradually shifts toward $T = 400$ μs, and at high porosity the η_U at $T = 800$ μs becomes the lowest among the three periods. For specimens with different pore sizes and shapes, the trends of U_v (Fig. 16(b)) and η_U (Fig. 16(c)) versus T are similar and their variation amplitudes are close; therefore, pore size and shape have almost no effect on the trends of strength, U_v, and η_U with T. In contrast, different porosities lead to pronounced differences in the trends of U_v and η_U with T.

Accordingly, when optimizing the characteristic frequency of drilling impact waves, the primary controlling pore parameter to consider is porosity. If the optimization objective is to reduce strength to facilitate rock breaking under a fixed impact amplitude, it is recommended to use characteristic periods of $T = 200$ and 800 μs and avoid $T = 400$ μs. If the optimization objective is to improve energy-use efficiency, the impact-wave period can be selected according to formation porosity. For the rock corresponding to this numerical study, when the porosity is less than 5%, a period of $T = 800$ μs or even longer may be used; when the porosity is greater than 5%, a period of $T = 800$ μs can be used to pursue the maximum rock-breaking efficiency and drilling energy utilization.

Table 4
Setting of impact parameters.

Pore parameters	Specimen number	Impact parameters
Porosity	A1-1, A1-2, A1-3, A1-4, A1-5	(T = 200, 400, 800 μs; $A_{\text{norm}} = 6$)
Porosity	A1-1, A1-2, A1-3, A1-4, A1-5	(T = 200 μs; A_{norm} = 6, 12, 18)
Pore size	B1-1, B1-2, B1-3, B2-1, B2-2, B2-3	(T = 200, 400, 800 μs; $A_{\text{norm}} = 6$)
Pore size	B1-1, B1-2, B1-3, B2-1, B2-2, B2-3	(T = 200 μs; A_{norm} = 6, 12, 18)
Pore shape	E1-1, E1-2, E1-3, E2-1, E2-2, E2-3	(T = 200, 400, 800 μs; $A_{\text{norm}} = 6$)
Pore shape	E1-1, E1-2, E1-3, E2-1, E2-2, E2-3	(T = 200 μs; A_{norm} = 6, 12, 18)

5.2. Dynamic mechanical response of specimens under the coupled influence of pore structure and amplitude of the impact stress wave

As shown in Fig. 17, under the three impact-amplitude ratios A_{norm} = 6, 12, 18, the normalized peak stress σ_{norm} increases markedly with increasing A_{norm}; this trend holds across different porosities (Fig. 17(a)), pore sizes (Fig. 17(b)), and pore shapes (Fig. 17(c)). However, the increment in σ_{norm} diminishes as porosity increases.

The energy dissipation density U_{v} increases with A_{norm}, with its maximum occurring at $A_{\text{norm}} = 18$ for all cases. The growth of U_{v} becomes smaller as porosity rises, and is largest at $\varphi_{\text{r}} \approx 1\%$, where U_{v} is about 1.5×10^7 J/cm^3. This indicates that the sensitivity of U_{v} to A_{norm} is porosity dependent. The optimum and trend of η_{U} with respect to A_{norm} are likewise porosity dependent: when $\varphi_{\text{r}} < 3\%$, η_{U} attains its maximum at $A_{\text{norm}} = 6$; when $\varphi_{\text{r}} > 5\%$, η_{U} decreases noticeably with increasing A_{norm}, and this decreasing trend becomes more pronounced as porosity increases. For specimens with different pore sizes and shapes, the U_{v} (Fig. 17(b)) and η_{U} (Fig. 17(c)) curves versus A_{norm} exhibit similar trends and comparable magnitudes; therefore, pore size and shape have little influence on the A_{norm} dependence of strength, U_{v}, and η_{U}. The porosity-dependent variation in η_{U} is mainly governed by pore-controlled stress-wave propagation and energy dissipation. With increasing porosity, the rock matrix becomes less compact and contains more voids, which enhances stress-wave scattering, reflection, and attenuation during transmission. Consequently, high-porosity specimens exhibit a lower transmitted-wave intensity and a shorter effective transmission stage, implying easier strain localization and earlier microcrack initiation that disrupt continuous energy transfer. By contrast, low-porosity specimens retain a denser, more stable load-bearing framework, allowing stress waves to propagate with slower attenuation and enabling a larger fraction of the input energy to be transmitted and utilized in driving macroscopic failure.

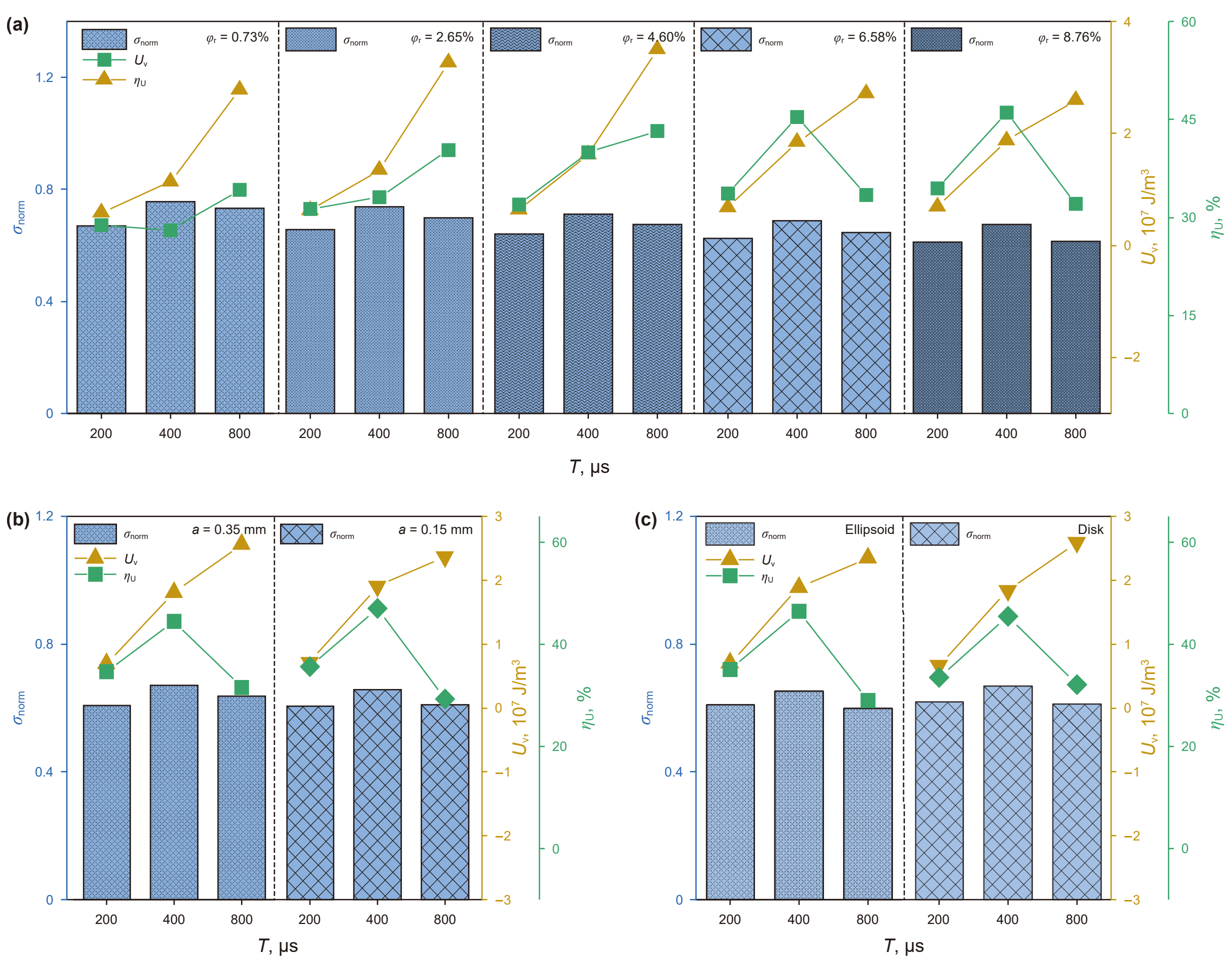

Fig. 16. The mechanical response of specimens with different pore parameters under different periodic shock waves. Bars denote σ_{norm}; lines show U_{v} and η_{U}. (**a**) Variation with porosity. (**b**) Variation with pore size at fixed φ_{r}. (**c**) Variation with pore shape at fixed φ_{r}.

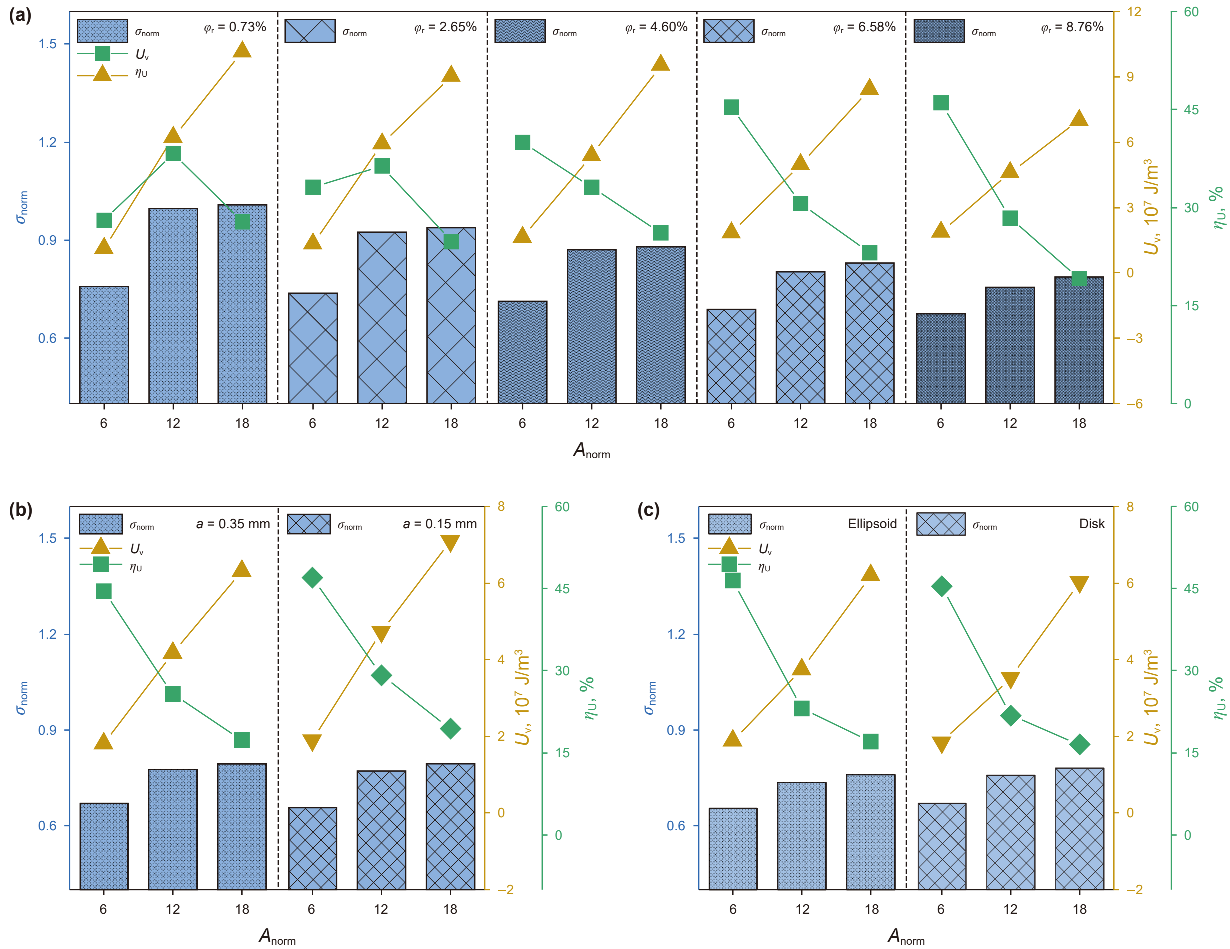

Fig. 17. The mechanical response of specimens with different pore parameters under different impact stress wave amplitudes. Bars denote σ_{norm}; lines show U_v and η_U. (**a**) Variation with porosity. (**b**) Variation with pore size at fixed φ_r. (**c**) Variation with pore shape at fixed φ_r.

As shown in Fig. 7, the difference in accumulated damage at 1040 μs among specimens with varying porosities further supports this mechanism. From an energy perspective, excessive incident energy in highly porous rocks tends to dissipate through non-destructive mechanisms such as pore collapse, microcrack extension, and internal frictional loss, leading to a reduction in η_U. Therefore, as porosity increases, adopting lower incident energy—i.e., a smaller A_{norm} and shorter T—is more effective in enhancing η_U. This mechanism reasonably explains the results in Figs. 16 and 17, where both the optimal stress-wave period and amplitude corresponding to maximum η_U decrease with increasing porosity.

Accordingly, impact wave amplitude optimization should treat porosity as the primary controlling parameter. For the rock type considered here, when porosity is less than 3% a recommended choice is $A_{norm} = 12$; when porosity is larger than 5%, reducing to $A_{norm} = 6$ can simultaneously yield a lower σ_{norm} and a higher η_U, thereby improving both rock-breaking efficiency and energy utilization.

6. Conclusion

This study establishes a parameterized modeling approach for porous rocks and develops a numerical simulation framework for split Hopkinson pressure bar (SHPB) tests under high strain-rate conditions to investigate the influence of pore structure on the dynamic mechanical response of rocks. Validation results demonstrate that the proposed method accurately reproduces the mechanical behavior of rocks under impact loading and effectively captures the damage evolution mechanisms governed by pore structures.

Based on this framework, a systematic investigation was conducted to examine the effects of four key pore parameters—porosity, pore size, aspect ratio, and orientation angle—on rock impact performance. The results indicate that porosity is the dominant factor controlling the dynamic mechanical response of rocks. Larger pore sizes tend to reduce rock strength but enhance energy storage capacity, while greater aspect ratio differences lead to more complex crack networks and increased energy dissipation. In particular, disk-shaped pores exhibit a pronounced synergistic effect between aspect ratio and orientation angle θ, indicating that pore geometry and orientation jointly regulate stress response behavior.

A further analysis indicates that porosity is the dominant factor governing impact load optimization. When the objective is to weaken rock strength, a loading period of 200 μs can be adopted; when aiming to maximize energy utilization efficiency, the loading period should be adjusted according to the porosity of the formation. In terms of amplitude selection, low-porosity formations are better suited to higher amplitudes ($A_{norm} = 12$), whereas high-porosity formations require lower amplitudes ($A_{norm} = 6$) to achieve a balance between strength reduction and energy efficiency.

CRediT authorship contribution statement

Zi-Zhen Wang: Writing – review & editing, Supervision, Funding acquisition, Conceptualization. **Wen-Sheng Zhang:** Writing – original draft, Software, Investigation, Formal analysis. **Yan-Bin Zang:** Supervision. **Xiao-Ao Liu:** Validation. **Wei-Dong Zhou:** Supervision, Resources.

Declaration of interests

The authors declare that they have no known competing financial interests or personal relationships that could have appeared to influence the work reported in this paper.

Acknowledgements

This work was supported by the National Natural Science Foundation of China (Grant No. 52374025), and the Fundamental Research Funds for the Central Universities (Nos. 24CX02011A, 24CX03016A). The authors gratefully acknowledge the experimental support and computational resources provided by the State Key Laboratory of Deep Oil and Gas, China University of Petroleum (East China).

References

Asadi, P., Fakhimi, A., Ashrafi, M.J., 2023. Dynamic tensile strength of rock specimens with different defect lengths. Eng. Fract. Mech. 284, 10425. https://doi.org/10.1016/j.engfracmech.2023.109245.
Bubeck, A., Walker, R.J., Healy, D., Dobbs, M., Holwell, D.A., 2017. Pore geometry as a control on rock strength. Earth Planet Sci. Lett. 457, 38–48. https://doi.org/10.1016/j.epsl.2016.09.050.
Chen, D.F., Xu, D.P., Ren, G.F., Jiang, Q., Liu, G.F., Wang, L.P., Li, N., 2019. Simulation of cross-correlated non-Gaussian random fields for layered rock mass mechanical parameters. Comput. Geotech. 112, 104–119. https://doi.org/10.1016/j.compgeo.2019.04.012.
Chen, R., Zhao, G., Xu, Y., Yao, W., Yao, W., Xia, K., 2024. Coupled hydraulic-mechanical experimental system for evaluating dynamic mechanical and transport behaviors of deep rocks. Exp. Mech. 64, 895–911. https://doi.org/10.1007/s11340-024-01063-z.
Du, K., Li, X., Tao, M., Wang, S., 2020. Experimental study on acoustic emission (AE) characteristics and crack classification during rock fracture in several basic lab tests. Int. J. Rock Mech. Min. Sci. 133, 104411. https://doi.org/10.1016/j.ijrmms.2020.104411.
Du, W., Zhang, D., Yu, B., 2023. Mechanical and fractal characteristics of sandstone with pre-existing fissures of different lengths under varying impact loads in SHPB tests. Theor. Appl. Fract. Mech. 125, 103884. https://doi.org/10.1016/j.tafmec.2023.103884.
Fakhimi, A., Gharahbagh, E.A., 2011. Discrete element analysis of the effect of pore size and pore distribution on the mechanical behavior of rock. Int. J. Rock Mech. Min. Sci. 48, 77–85. https://doi.org/10.1016/j.ijrmms.2010.08.007.
Fredrich, J.T., 1999. 3D imaging of porous media using laser scanning confocal microscopy with application to microscale transport processes. Phys. Chem. Earth Solid Earth Geodes. 24 (7), 551–561. https://doi.org/10.1016/S1464-1895(99)00079-4.
Gao, F., Stead, D., 2014. The application of a modified Voronoi logic to brittle fracture modelling at the laboratory and field scale. Int. J. Rock Mech. Min. Sci. 68, 1–14. https://doi.org/10.1016/j.ijrmms.2014.02.003.
Griffiths, L., Heap, M.J., Xu, T., Chen, C., Baud, P., 2017. The influence of pore geometry and orientation on the strength and stiffness of porous rock. J. Struct. Geol. 96, 149–160. https://doi.org/10.1016/j.jsg.2017.02.006.
Hao, Y., Hao, H., Li, Z.X., 2013. Influence of end friction confinement on impact tests of concrete material at high strain rate. Int. J. Impact Eng. 60, 82–106. https://doi.org/10.1016/j.ijimpeng.2013.04.008.
He, J., Li, X., Yin, C., Zhang, Y., Lin, C., 2020. Propagation and characterization of the micro cracks induced by hydraulic fracturing in shale. Energy 191, 116449. https://doi.org/10.1016/j.energy.2019.116449.
Hu, A., Xue, G., Shang, Z., Cao, Zhe, Wang, X., Fu, Y., Huang, X., 2023. Study on pore structure and the mechanical properties of sandstone-concrete binary under freeze-thaw environment. Sci. Rep. 13 (1), 18280. https://doi.org/10.1038/s41598-023-45576-4.
Hu, N., Liu, X., Wang, Y., 2022. Effect of original pores on dynamic characteristics of granite under cyclic impact loading. In: ISRM 4th International Conference on Rock Dynamics. https://doi.org/10.1201/9781003359142-21.
Hu, R., Han, J., Wang, C., Zhu, J., Hu, D., 2025. Multiscale pore/throat characterization in tight sandstone formation with multi-threshold image segmentation algorithm. Front. Earth Sci. 13. https://doi.org/10.3389/feart.2025.1576484.
Jani, A., Dehkouhneh, H.Z., Varnamkhasti, S.K., Farhadi, A., Moghadam, M.B., 2023. Evaluation of porous media using digital core analysis by pore network modeling method: A comprehensive review. J. Chem. Petrol. Eng. 57 (2), 249–285. https://doi.org/10.22059/jchpe.2023.357295.1428.
Jiang, C., Niu, B., Yin, G., Zhang, D., Yu, T., Wang, P., 2019. CT-based 3D reconstruction of the geometry and propagation of hydraulic fracturing in shale. J. Petrol. Sci. Eng. 179, 899–911. https://doi.org/10.1016/j.petrol.2019.04.103.
Kim, E., Changani, H., 2016. Effect of water saturation and loading rate on the mechanical properties of red and Buff Sandstones. Int. J. Rock Mech. Min. Sci. 88, 23–28. https://doi.org/10.1016/j.ijrmms.2016.07.005.
Kranz, R.L., 1983. Microcracks in rocks: A review. Tectonophysics 100 (1–3), 449–480. https://doi.org/10.1016/0040-1951(83)90198-1.
Lang, Y., Liang, Z., Dong, Z., 2024. Three-dimensional finite element simulation and reconstruction of jointed rock models using CT scanning and photogrammetry. J. Rock Mech. Geotech. Eng. 16, 1348–1361. https://doi.org/10.1016/j.jrmge.2023.08.008.
Li, D., Han, Z., Sun, X., Zhou, T., Li, X., 2018. Dynamic mechanical properties and fracturing behavior of marble specimens containing single and double flaws in SHPB tests. Rock Mech. Rock Eng. 52, 1623–1643. https://doi.org/10.1007/s00603-018-1652-5.
Li, J., Dai, L., Wang, S., Liu, Y., Sun, Y., Wang, J., Zhang, A., 2024. Theoretical and numerical analysis of the rock breaking process by impact hammer. Powder Technol. 448, 120254. https://doi.org/10.1016/j.powtec.2024.120254.
Li, J.C., Li, N.N., Li, H.B., Zhao, J., 2017. An SHPB test study on wave propagation across rock masses with different contact area ratios of joint. Int. J. Impact Eng. 105, 109–116. https://doi.org/10.1016/j.ijimpeng.2016.12.011.
Liu, Q., Jiang, Y., Wu, Z., He, J., 2018. A Voronoi element based-numerical manifold method (VE-NMM) for investigating micro/macro-mechanical properties of intact rocks. Eng. Fract. Mech. 199, 71–85. https://doi.org/10.1016/j.engfracmech.2018.05.010.
Liu, Q., Jiang, Y., Wu, Z., Xu, X., Liu, Q., 2017. Investigation of the rock fragmentation process by a single TBM cutter using a voronoi element-based numerical manifold method. Rock Mech. Rock Eng. 51, 1137–1152. https://doi.org/10.1007/s00603-017-1381-1.
Liu, S., Huang, Z., 2021. Analysis of strength property and pore characteristics of Taihang limestone using X-ray computed tomography at high temperatures. Sci. Rep. 11, 13478. https://doi.org/10.1038/s41598-021-92928-z.
Ng, K., Santamarina, J.C., 2023. Mechanical and hydraulic properties of carbonate rock: The critical role of porosity. J. Rock Mech. Geotech. Eng. 15, 814–825. https://doi.org/10.1016/j.jrmge.2022.07.017.
Ostoja-Starzewski, M., 1998. Random field models of heterogeneous materials. Int. J. Solid Struct. 35 (19), 2429–2455. https://doi.org/10.1016/S0020-7683(97)00144-3.
Pan, Y., Wu, G., He, L., Zhao, Z., 2023. Combined effects of porosity and degree of saturation on the mechanical properties and deformation behaviour of rocks. Q. J. Eng. Geol. Hydrogeol. 56 (2), qjegh2020–qjegh074. https://doi.org/10.1144/qjegh2020-074.
Pang, M., Ba, J., Carcione, J.M., Balcewicz, M., Siegert, M., Tang, G., Saenger, E.H., 2025. Structural and elastic properties of carbonate rocks with different pore types based on digital and theoretical rock physics. J. Geophys. Res. Solid Earth 130 (3), e2024JB030538. https://doi.org/10.1029/2024JB030538.
Pang, M., Ba, J., Carcione, J.M., Saenger, E.H., 2024. Combined acoustical–electrical modeling for tight sandstones verified by laboratory measurements. Int. J. Rock Mech. Min. Sci. 176, 105682. https://doi.org/10.1016/j.ijrmms.2024.105682.
Queiroz, L.E., Grana, D., Fernandes, C.P., Mukerji, T., Figueiredo, L.P., Mantovani, I.F.M., 2025. Estimation of equivalent pore aspect ratio in rock physics models and validation using digital rocks. Geosciences 15, 67. https://doi.org/10.3390/geosciences15020067.
Rodríguez, P., Celestino, T.B., 2019. Application of acoustic emission monitoring and signal analysis to the qualitative and quantitative characterization of the fracturing process in rocks. Eng. Fract. Mech. 210, 54–69. https://doi.org/10.1016/j.engfracmech.2018.06.027.
Sadeghnejad, S., Gostick, J., 2020. Multiscale reconstruction of vuggy carbonates by pore-network modeling and image-based technique. SPE J. 25 (1), 253–267. https://doi.org/10.2118/198902-PA.
Song, Y., Ma, H., Yang, J., Zheng, J., Yang, J., Bao, W., 2022. Dynamic mechanical behaviors and failure mechanism of lignite under SHPB compression test. Sustainability 14 (17), 10528. https://doi.org/10.3390/su141710528.
Stopka, G., Gieleta, R., Panowicz, R., Wałach, D., Kaczmarczyk, G.P., 2024. High strain rate response of sandstones with different porosity under dynamic loading using split hopkinson pressure bar (SHPB). Appl. Sci. 14 (12), 5347. https://doi.org/10.3390/app14125347.
Sulieman, H., Jouini, M.S., Alsuwaidi, M., Al-Shalabi, E.W., Al Jallad, O.A., 2024. Multiscale investigation of pore structure heterogeneity in carbonate rocks using digital imaging and SCAL measurements: A case study from Upper Jurassic limestones, Abu Dhabi, UAE. PLoS One 19 (2), e0295192. https://doi.org/10.1371/journal.pone.0295192.
Sun, W., Ren, X., Zhang, J., Xu, H., 2025. Numerical simulation of crack propagation in rocks with random pores based on improved smoothed particle hydrodynamics method. Appl. Sci. 15, 1826. https://doi.org/10.3390/app15041826.
Wang, W., Liu, G., Li, J., Zha, C., Lian, W., 2021. Numerical simulation study on rock-breaking process and mechanism of compound impact drilling. Energy Rep. 7, 3137–3148. https://doi.org/10.1016/j.egyr.2021.05.040.
Wang, Y., Zhao, L., Han, D., Qin, X., Ren, J., Wei, Q., 2020. Micro-mechanical analysis of the effects of stress cycles on the dynamic and static mechanical properties

of sandstone. Int. J. Rock Mech. Min. Sci. 134, 104431. https://doi.org/10.1016/j.ijrmms.2020.104431.
Wang, Z., Yang, S., Li, L., Tang, Y., Xu, G., 2021. A 3D Voronoi clump based model for simulating failure behavior of brittle rock. Eng. Fract. Mech. 248, 107720. https://doi.org/10.1016/j.engfracmech.2021.107720.
Xiao, N., Chen, J.Q., Qiu, X., Huang, F., Ling, T.H., 2025. Study on the relationship between porosity and mechanical properties based on rock pore structure reconstruction model. Appl. Sci. 15 (13), 7247. https://doi.org/10.3390/app15137247.
Xie, L.X., Lu, W.B., Zhang, Q.B., Jiang, Q.H., Chen, M., Zhao, J., 2017. Analysis of damage mechanisms and optimization of cut blasting design under high in-situ stresses. Tunn. Undergr. Space Technol. 66, 19–33. https://doi.org/10.1016/j.tust.2017.03.009.
Yang, J., Mu, Z.L., Yang, S.Q., 2020. Experimental study of acoustic emission multi-parameter information characterizing rock crack development. Eng. Fract. Mech. 232, 107045. https://doi.org/10.1016/j.engfracmech.2020.107045.
Yang, S.Q., Li, Y., Ma, G.W., Sun, B.W., Yang, J., Xu, J., Dai, Y.H., 2023. Experiment and numerical simulation study of dynamic mechanical behavior of granite specimen after high temperature treatment. Comput. Geotech. 154, 105111. https://doi.org/10.1016/j.compgeo.2022.105111.
Yang, Y., Li, Q., Qiao, L., 2023. Review of SHPB dynamic load impact test characteristics and energy analysis methods. Processes 11 (10), 3029. https://doi.org/10.3390/pr11103029.
Yao, J., Liu, L., Yang, Y., Sun, H., Zhang, L., 2023. Characterizing multi-scale shale pore structure based on multi-experimental imaging and machine learning. Nat. Gas. Ind. B 10 (4), 361–371. https://doi.org/10.1016/j.ngib.2023.07.005.
Yun, T.S., Jeong, Y.J., Kim, K.Y., Min, K.B., 2013. Evaluation of rock anisotropy using 3D X-ray computed tomography. Eng. Geol. 163, 11–19. https://doi.org/10.1016/j.enggeo.2013.05.017.
Zambrano, M., Volatili, T., Mancini, L., Pitts, A.D., Giorgioni, M., Tondo, E., 2021. Pore-scale dual-porosity and dual-permeability modeling in an exposed multi-facies porous carbonate reservoir. Mar. Petrol. Geol. 128, 105004. https://doi.org/10.1016/j.marpetgeo.2021.105004.
Zhang, Q.B., Zhao, J., 2014. A review of dynamic experimental techniques and mechanical behaviour of rock materials. Rock Mech. Rock Eng. 47, 1411–1478. https://doi.org/10.1007/s00603-013-0463-y.
Zhao, L., Deng, M., Wang, X., Huang, D., Zuo, S., 2022. Stochastic model generation of porous rocks and study on 2D pore morphology influencing rock strength and stiffness. Front. Mater. 9, 956742. https://doi.org/10.3389/fmats.2022.956742.
Zhao, Y., Qin, W., Jin, A., Wu, H., Chen, Z., 2024. Research and analysis of the impact of the pore structure on the mechanical properties and fracture mechanism of sandstone. Mater. Today Commun. 38, 107753. https://doi.org/10.1016/j.mtcomm.2023.107753.
Zhou, Y., Sheng, Q., Li, N., Fu, X., 2020. The influence of strain rate on the energy characteristics and damage evolution of rock materials under dynamic uniaxial compression. Rock Mech. Rock Eng. 53 (8), 3823–3834. https://doi.org/10.1007/s00603-020-02128-w.
Zou, C., Li, J., Liu, K., Zhao, X., 2023. Dynamic cracking process of rock interpreted by localized strain-rate, rate-dependent strength field and transition strain-rate. Int. J. Rock Mech. Min. Sci. 163, 105340. https://doi.org/10.1016/j.ijrmms.2023.105340.